

GEANT4 SIMULATIONS OF β -DELAYED
PARTICLE EMISSION OF ^{11}BE IN A
LINEAR PAUL TRAP

by

Brandon J. Boucher

© Copyright by Brandon J. Boucher, 2020

All Rights Reserved

A thesis submitted to the Faculty and the Board of Trustees of the Colorado School of Mines in partial fulfillment of the requirements for the degree of Master of Science (Applied Physics).

Golden, Colorado

Date _____

Signed: _____

Brandon J. Boucher

Signed: _____

Dr. Kyle G. Leach
Thesis Advisor

Signed: _____

Dr. Aaron T. Gallant
Thesis Advisor

Golden, Colorado

Date _____

Signed: _____

Dr. Uwe Greife
Professor and Head
Department of Physics

ABSTRACT

The phenomenon of nuclear halos occurs when the matter radius of near-dripline nuclei are extended due to very weakly bound neutrons (or protons). If the Q-value of the β decay is greater than the separation energy of the outermost nucleon, the nucleon may be emitted separately from the core. One very unique case of β -delayed particle emission is ^{11}Be as its branching ratio to the exotic states is greater than expected as a result of a nonspherical deformation in its core, ^{10}Be . The newly proposed BeTrap, a linear Paul trap specially designed for Beryllium decay, was constructed in the simulation toolkit, GEANT4. The input parameters of the decay particles were determined by the decay rate equation developed in ref [1] which functions to ensure triple correlation between the β particle, neutrino and emitted particle. This thesis provides verification of the differentiation of the time-of-flight difference profiles of the β and β -delayed channels. Additionally, this work determines the influence of the ion cloud size on the detected difference in hit positions and the parameters of a kinematic cut to suppress the background coincidences. This work provides the foundation for future experimental expectations.

TABLE OF CONTENTS

ABSTRACT	iii
LIST OF FIGURES AND TABLES	vii
LIST OF SYMBOLS	ix
LIST OF ABBREVIATIONS	x
ACKNOWLEDGMENTS	xi
DEDICATION	xii
CHAPTER 1 INTRODUCTION	1
1.1 β Decay	1
1.1.1 Fermi Theory of β decay	2
1.1.2 Angular Momentum and Parity Selection Rules	5
1.1.3 β -Delayed Particles	6
1.2 β -Delayed Particle Emission of ^{11}Be	8
1.3 Decay Rate Equation	10
1.4 Previous Measurements of the βp channel of ^{11}Be	11
CHAPTER 2 ION TRAPS AND THE DETECTION OF LOW ENERGY NUCLEAR RECOILS	14
2.1 Ion trap techniques	14
2.2 Electromagnetic traps for charged particles	17
2.3 BeTrap	19
CHAPTER 3 SIMULATION METHOD	22

3.1	GEANT4 and ROOT	22
3.1.1	Geometry and Visualization of the Ion Trap	23
3.1.2	Detection Efficiency	24
3.2	Decay Rate Equation	25
3.2.1	Decay Rate Maximum	26
3.2.2	β - ν Correlation	26
3.2.3	Fermi Function	28
3.3	Initial Set-up and Variable Ion Cloud Size	28
3.4	Verification of the β , ν and α Energy Distributions	29
3.4.1	Excitation of ^{11}B	29
3.4.2	β and ν Energy Distributions	31
3.4.3	Emitted Particle Energy Distribution	33
3.4.4	Galilean Transformation	33
CHAPTER 4 SIMULATION RESULTS AND DISCUSSION		34
4.1	ToF Difference Profiles	34
4.2	Kinematic Cuts	39
4.3	Cloud Size	42
CHAPTER 5 CONCLUSION		45
REFERENCES CITED		47
APPENDIX A DERIVATION OF THE ENERGY OF THE NEUTRINO AND β -DELAYED PARTICLE		53
A.1	Derivation of the neutrino energy	53
A.2	Derivation of the energy of the β -delayed particle	54

APPENDIX B DETAILS ON THE CONFIRMATION OF THE HALO STRUCTURE OF ^{11}Be	55
APPENDIX C DETAILED ANALYSIS OF A SPECTRAL FUNCTION	56
APPENDIX D DISCUSSION OF THE LINEAR PAUL TRAP'S EFFECT ON THE SECOND-ORDER DOPPLER SHIFT EFFECTS	58
APPENDIX E βP DELAYED DECAY CHANNEL HISTOGRAMS	59
APPENDIX F DISCUSSION OF $\beta\alpha$ TOF DIFFERENCE PROFILE	62

LIST OF FIGURES AND TABLES

Figure 1.1	Electron momentum and energy distributions from Equation 1.9	4
Figure 1.2	Momentum and kinetic energy spectra of electrons and positrons	6
Figure 1.3	Decay scheme for β delayed particle emission	7
Figure 1.4	Competition between $s_{1/2}$ and $p_{1/2}$ levels	9
Figure 1.5	^{11}Be decay scheme	10
Figure 1.6	Energy distribution of β -delayed protons	12
Figure 2.1	Potential well of RF-quadrupole ion trap	15
Figure 2.2	Radial density distribution in a Paul trap for different temperatures	16
Figure 2.3	Equipotential lines for the electrode configuration	18
Figure 2.4	Ion trap saddle potential	18
Figure 2.5	An Autodesk Fusion 360 cutaway model of the BeTrap, adopted from ref	19
Figure 2.6	MCP electron detection efficiency for energies 3 keV to 2.6 MeV	20
Figure 2.7	MCP detection efficiency for ions with energies 0 keV and 4.75 keV	21
Figure 3.1	Simulated visualization of the ion trap using GEANT4	23
Figure 3.2	Simulated visualization of the ion trap using GEANT4	24
Figure 3.3	Absolute detection efficiency of β particles with analytical model fit	25
Figure 3.4	Simulated Distribution of $\hat{p} \cdot \hat{k}$ for a Gamow-Teller transition	27
Figure 3.5	Observed energy and an R matrix fit vs Simulated distribution	30
Figure 3.6	Simulated Distribution of ^{11}B Excitation Energy	31
Figure 3.7	Simulated Distribution of Q-values for the $\beta\alpha$ decay channel	31

Figure 3.8	Simulated distribution of electron and neutrino energies	32
Figure 4.1	Simulated ToF of the $\beta\alpha$ channel	35
Figure 4.2	Simulated ToF of the βp channel	36
Figure 4.3	Simulated ToF of the β decay channel	37
Figure 4.4	Simulated distribution for the $\beta\alpha$, βp and bound state β decay	38
Figure 4.5	Cartoon illustrating a back-to-back detection	39
Figure 4.6	Simulated detected difference in hit positions for each channel	41
Figure 4.7	Simulated distribution of the difference in hit positions, $\beta\alpha$ channel	42
Figure 4.8	Simulated Comparison of the difference in hit position to cloud size	43
Figure 4.9	Simulated Comparison of the average ToF with varying ion cloud size	44
Figure B.1	Comparison of cross sections	55
Figure E.1	Simulated distribution of excitation energy for the βp decay channel	59
Figure E.2	Simulated distribution of Q-value for the βp decay channel	60
Figure E.3	Simulated distribution of neutrino energy for the βp decay channel	60
Figure E.4	Simulated distribution of electron energy for the βp decay channel	61
Figure E.5	Simulated distribution of proton energy for the βp decay channel	61
Figure F.1	Simulated distribution of ToF difference profile for the $\beta\alpha$ channel	62
Table C.1	Factors incorporated in the majority of terms in Equation C.1	57

LIST OF SYMBOLS

Speed of light	c
The imaginary unit	i
Neutrino	ν
Anti-Neutrino	$\bar{\nu}$
Electron	e^{-}
Positron	e^{+}

LIST OF ABBREVIATIONS

Time-of-Flight	ToF
Electron Capture	EC
Radiofrequency	RF
Full Width at Half Maximum	FWHM
Microchannel Plate	MCP

ACKNOWLEDGMENTS

I would like to thank the academy for granting me this prestigious thesis. Additionally, I would like to thank Dr. Kyle Leach and Dr. Aaron Gallant for making this possible and providing guidance through every step of this project. I would also like to thank my fellow graduate students for helping me with their experience. Namely, I would like to thank Connor Bray for his help with C++, GEANT4 and ROOT. I would also like to thank Isabella Morfe for her help with correcting my inability to discern where commas should go. Lastly, I would like to thank my parents for supporting me and always pushing me to do my best.

Abandon all hope ye who enter here

CHAPTER 1

INTRODUCTION

The phenomenon of nuclear halos occurs when the matter radius of near-dripline nuclei are extended due to very weakly bound neutrons (or protons) sitting in a low orbital angular momentum orientation. If the Q-value of the β decay exceeds the separation energy of the halo nucleon, the nucleon may be emitted from the core. An interesting case is the decay of the neutron-rich halo nucleus ^{11}Be . As a result of a nonspherical shape deformation of the core, ^{10}Be , the parity of ^{11}Be is such that the branching ratios for the $\beta\alpha$ and βp channels are higher than expected [2]. This makes ^{11}Be an excellent candidate for the investigation of β -delayed particle emission. The goal of this thesis is to simulate the detection of these rare β -delayed decay channels in a newly proposed β decay linear Paul trap specifically designed for beryllium decay (BeTrap), to garner a better understanding of β decay in general [3].

1.1 β Decay

β decay is a radioactive decay which stems from the transformation of either a proton or neutron into the other and the emission of a β particle and neutrino/antineutrino. There are three forms of β decay: β^- , β^+ and electron capture (EC) [4, 5]. In β^- decay, a bound neutron is converted into a proton with the emission of an electron and anti-neutrino [4]. Equation 1.1 defines β^- where an electron, e^- , and antineutrino, $\bar{\nu}_e$, are emitted to conserve charge and lepton number in the decay [5, 6].



In the same manner, β^+ is the transformation of a proton into a neutron with the emission of a positron and a neutrino, Equation 1.2 [4, 5].



Finally, Equation 1.3 defines EC, the third form of β decay [5].

$${}^A_Z X_N + e^- \rightarrow {}^A_{Z-1} W_{N+1} + \nu_e \quad (1.3)$$

If the small difference between the parent and daughter atomic binding energies is neglected, the Q-values for each form of β decay can be written in terms of their atomic masses [4]. Equation 1.4 depicts the Q-values using natural units for β^- , β^+ and EC, respectively [4, 5].

$$\begin{aligned} Q_{\beta^-} &= M({}^A_Z X_N) - M({}^A_{Z+1} Y_{N-1}) \\ Q_{\beta^+} &= M({}^A_Z X_N) - M({}^A_{Z-1} W_{N+1}) - 2m_e \\ Q_{EC} &= M({}^A_Z X_N) - M({}^A_{Z-1} W_{N+1}) \end{aligned} \quad (1.4)$$

The energy released is shared between the β particle, the neutrino and the daughter nucleus; therefore, the Q-value can be rewritten to reflect this, Equation 1.5, where T_β , T_ν and T_{recoil} are the kinetic energies of the β particle, neutrino and recoil daughter nucleus, respectively. E_D^* and E_{DA}^* are the excitation energies of the daughter nucleus and the daughter atom, respectively [5].

$$Q_\beta = T_\beta + T_\nu + T_{recoil} + E_D^* + E_{DA}^* \quad (1.5)$$

Assuming the mass of the neutrino is zero, Equation 1.6 defines the energy of neutrino in the rest frame of the parent. The derivation of this equation can be found in Appendix A.

$$E_\nu = \frac{m_{recoil}^2 - m_{parent}^2 - m_\beta^2 + 2(m_{parent} E_\beta)}{2(E_\beta - m_{parent} - \vec{p}_\beta \cdot \hat{p}_\nu)} \quad (1.6)$$

1.1.1 Fermi Theory of β decay

One of the defining features of any radioactive decay is the decay rate or transition rate. For β decay, the decay rate was determined using time-dependent perturbation theory by Fermi [7, 8]. Equation 1.7 is Fermi's Golden Rule where Γ is the transition rate, M_{fi} is the transition matrix element and $\rho(E_f)$ is the density of final states as a function of the final energy [4].

$$\Gamma = \frac{2\pi}{\hbar} |M_{fi}|^2 \rho(E_f) \quad (1.7)$$

Equation 1.8 defines the transition matrix element which functions to connect the initial and final states [4].

$$M_{fi} = \langle f | M | i \rangle = g \int [\psi_f^* \phi_\beta^* \phi_\nu^*] O_x \psi_i dv \quad (1.8)$$

M_{fi} was determined to take the form of Equation 1.8, where the coefficient, g , determines the strength of the interaction [4]. The portion of Equation 1.8 in brackets represents the total system; ψ_f , ϕ_β and ϕ_ν represent the final state of the nucleus, β particle and neutrino, respectively. O_x is a mathematical operator appropriate to one of the five possible forms of interaction: scalar (S), polar vector (V), tensor (T), axial vector (A) or pseudoscalar (P) acting on the initial state, ψ_i [9]. From experimentation focused on the symmetries and spatial properties of the decay products, β decay was determined to take a V-A form [4]. One of the difficulties in using Fermi's Golden Rule is the determination of M_{fi} .

The final density of states is dependent on the final states accessible to the decay products. Reference [4] gives the derivation of the final density by matching the shape of the energy spectra for the electron and neutrino. Equation 1.9 displays the electron energy spectra as a function of its kinetic energy, where C is a constant, T_e is the kinetic energy of the electron and Q is the Q-value [4]. Figure 1.1 displays the expected electron spectra as a function of its momentum and energy derived from Equation 1.9.

$$N(T_e) = \frac{C}{c^5} (T_e^2 + 2T_e m_e c^2)^{1/2} (Q - T_e)^2 (T_e + m_e c^2) \quad (1.9)$$

Equation 1.9 and Figure 1.1 represent the spectrum shape; however, its derivation doesn't take into account other effects including the Coulomb effect. Equation 1.10 is the number of electrons with momentum p in the interval p and $p + dp$ [10].

$$N(p_e) dp_e = \frac{g^2}{2\pi^3} p_e^2 p_\nu^2 F(Z, W_e) C(W_e) dp_e \quad (1.10)$$

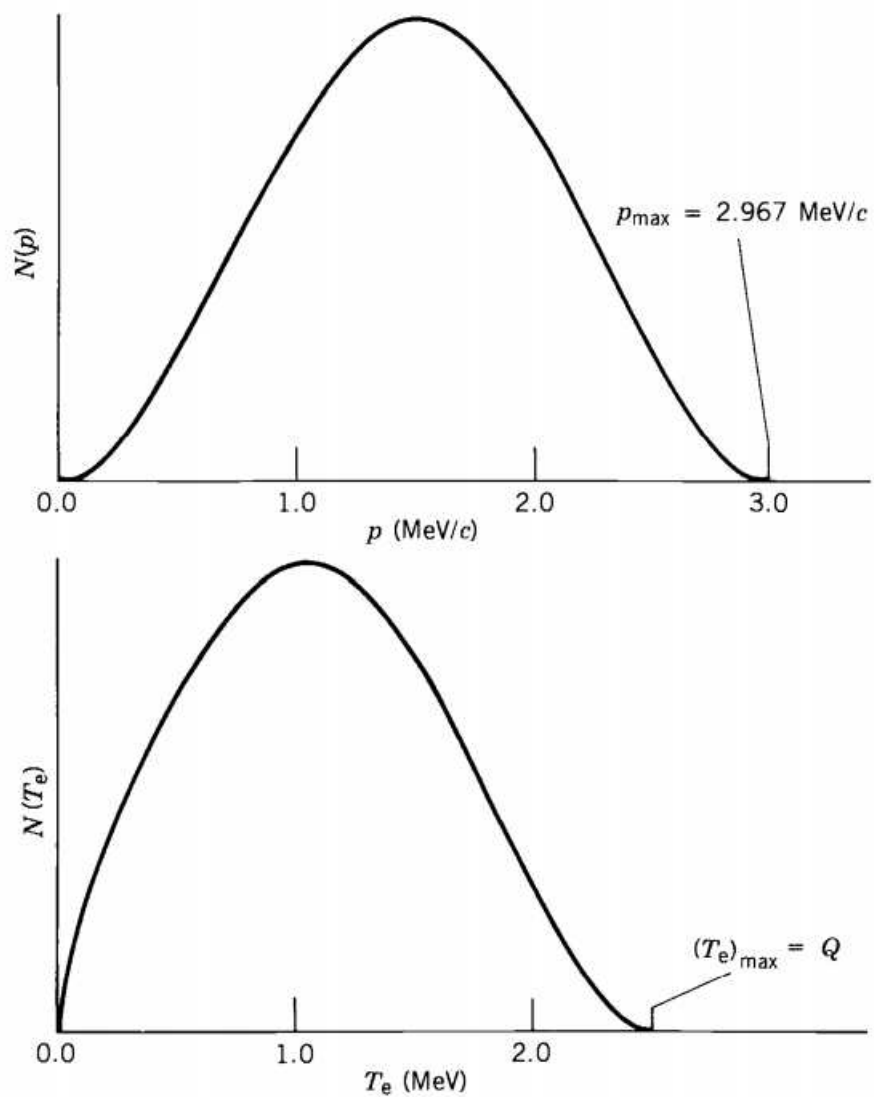


Figure 1.1: Electron momentum (top) and energy (bottom) distributions from Equation 1.9 adopted from ref [4]

From Equation 1.10, g is the weak interaction coupling strength, p_e is the electron momentum, p_ν is the neutrino momentum, Z is the atomic number of the daughter nucleus and W_e is the total electron energy [10]. Lastly, $F(Z, W_e)$ is the Fermi function which is derived from the quantum mechanical calculation of the effect of the nuclear Coulomb field on the electron wave function [4]. This effect is the electromagnetic interaction between the β particles and the nucleus [10]. Equation 1.11 is a non-relativistic calculation of the Fermi function as a function of the proton number of the daughter nucleus, Z , and the momentum of the β particle, η [9].

$$F_N(Z, \eta) \approx \frac{2\pi y}{1 - e^{-2\pi y}} \text{ where } y = \frac{\pm Ze^2 W}{\hbar c \eta} \quad (1.11)$$

From Equation 1.11, $e^2/\hbar c$ is the fine-structure constant, Z is the nuclear charge and W is the energy of the electron [9]. Figure 1.2 displays the electron energy and momenta emitted in the decay of ^{64}Cu with the inclusion of the Fermi function depending on the charge of the emitted lepton.

1.1.2 Angular Momentum and Parity Selection Rules

The selection rules for β decay are dependent on the angular momentum and parity of the states. If the electron and neutrino are created at the origin, then the only change in the angular momentum can result from the spins of both particles. Both the electron and neutrino have spins of $1/2$, meaning they are either parallel or antiparallel. If antiparallel the decay is referred to as a Fermi decay; parallel, Gamow-Teller [4]. If the electron and neutrino carry no orbital angular momentum, the parity of the initial and final states must be the same. If there is either a change in the nuclear spin of 0 or 1 and the parity doesn't change, this is considered an allowed β decay.

As opposed to allowed decays, forbidden decays typically result from a difference in parity. In order to have a change in parity, the electron and neutrino must have an odd value of the orbital angular momentum relative to the nucleus [4]. If the angular orbital momentum of the decay is 1 relative to 0, it is considered first-forbidden. For other odd values relative to

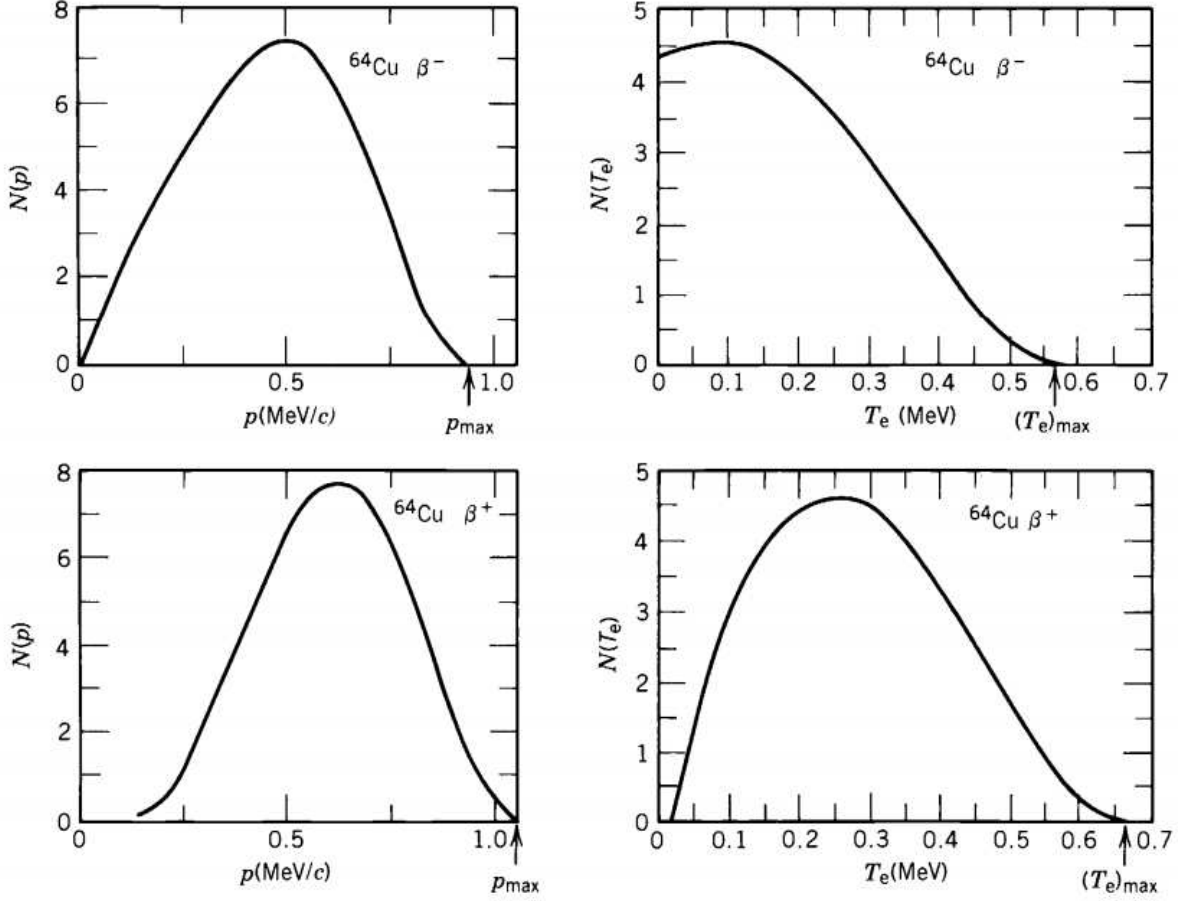


Figure 1.2: Momentum and kinetic energy spectra of electrons (top, β^-) and positrons (bottom, β^+) emitted in the decay of ^{64}Cu adopted from ref [4]

the nucleus, each is correspondingly forbidden and as the relative value increases, as does the unlikelihood of a decay to that state [4].

1.1.3 β -Delayed Particles

In exotic cases with large decay Q-values, some nuclei emit a nucleon after β decaying to a high enough excited state in the daughter nucleus. Figure 1.3 schematically depicts a β decay of the precursor and the emission of a nucleon to the daughter. The process depicted in Figure 1.3 can occur so long as the Q-value of the β decay is greater than the nucleon separation energy [4]. The nucleon separation energy is the amount of energy that is needed to remove a nucleon from a nucleus, analogous to ionization energy in atomic physics [4].

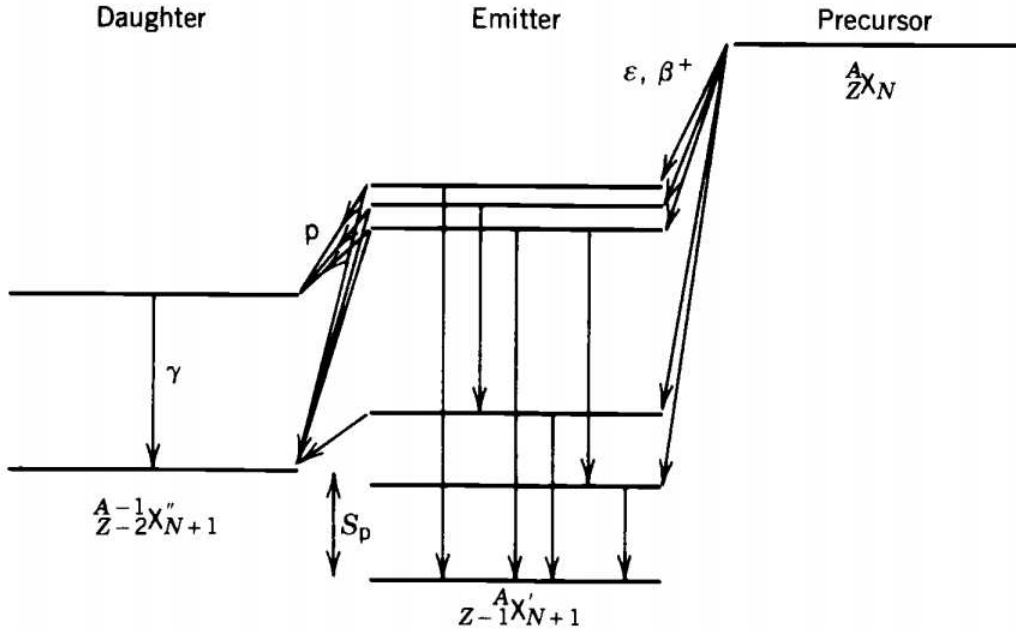


Figure 1.3: Decay scheme for β delayed particle emission adopted from [4]

This is well depicted in the nuclear shell model, suggesting outermost nucleons in a nucleus can be thought of as orbiting in subshells [4]. Nuclei further from the valley of stability have loosely-bound nucleons in subshells with lesser separation energy. Nuclei closer to the driplines will therefore have a greater likelihood of β -delayed nucleon emission [11].

Another characteristic of β decay far from the valley of stability is the number of decay channels open [12]. β -delayed particle emission is not exclusively the emission of a singular nucleon, and as a result of the lower separation energy it becomes possible for many different particles to be emitted [12]. These potential decay paths include $\beta\gamma$, βp , βn , $\beta\alpha$, βt , βd , βxp and βxn with $x = 2, 3, \dots$ and many other exotic decay channels [12]. However, there are physical limitations to the possibility of β -delayed particle emission including isospin and spin. Isospin is defined as a vector assigned to a nucleon with two different states, the proton and neutron [4]. Isospin and its selection rules mirror spin as discussed earlier in the chapter, such as the Fermi matrix element is forbidden unless the change in angular momentum is zero [4].

Lastly, the energy of the emitted particle can be determined using a combination of the conservation of energy and momentum. The derivation for the energy of the emitted particle is found in Appendix A. Equation 1.12 displays the result, the energy of the emitted particle as a function of the masses of the precursor, daughter and emitter.

$$E_{emitted} = \frac{m_{precursor}^2 + m_{daughter}^2 - m_{emitter}^2}{2m_{precursor}} \quad (1.12)$$

1.2 β -Delayed Particle Emission of ^{11}Be

^{11}Be is unique in that it has an unusually high branching ratio to the βp decay channel for a nucleus on the neutron rich side resulting from its halo structure [13]. Naively, this can be thought of as a nucleon orbiting around a tightly bound core. This neutron halo is characterized as being loosely bound with a neutron separation energy less than 1 MeV [14]. This allows for the potential of the halo neutron decaying separately from the core and emitted if the decay proceeds through a state above the separation energy of the emitted particle [3, 4]. More information about the confirmation of the halo structure of ^{11}Be is provided in Appendix B.

What differentiates ^{11}Be from other halo nuclei is a deformation of its core, ^{10}Be , resulting in an even parity ground state, which defies what the shell model predicts [15–17]. This deviation results from the $s_{1/2}$ orbital sitting 0.21 MeV below the $p_{1/2}$ orbital. Figure 1.4 depicts the difference between the energy levels of $s_{1/2}$ and $p_{1/2}$ orbitals for ^{11}Be , ^{12}B and ^{13}C [17]. The level difference results from competition between orbitals which is dependent on the proton configuration [17]. Later, the parity was analyzed and understood using direct computation of level structures using variational calculations with deformed wave functions through the projected Hartree-Fock method [18–20].

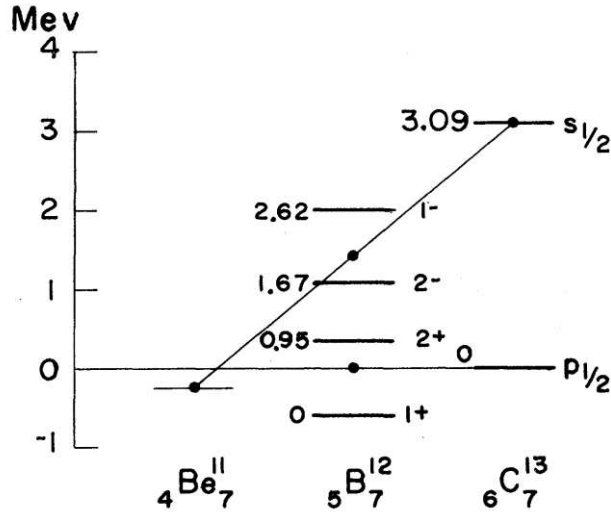


Figure 1.4: Competition between $s_{1/2}$ and $p_{1/2}$ levels adopted from [17]

The importance of the even parity is depicted in Figure 1.5, the decay scheme of ${}^{11}\text{Be}$, where the lowest four energy levels of ${}^{11}\text{B}$ including the ground state are odd parity [21]. This implies they are considered forbidden states as previously discussed earlier in the chapter. The combination of the halo neutron and the resulting even parity increases the branching ratio of the βp channel, making ${}^{11}\text{Be}$ important to the study of β -delayed particle emission.

${}^{11}\text{Be}$ has four energetically possible β -delayed channels, $\beta\alpha$, βt , βp and βn with Q-values of 2845.2 ± 0.2 keV, 285.7 ± 0.2 keV, 280.7 ± 0.3 keV and 55.2 ± 0.2 keV, respectively [3, 23]. However, for the purposes of this thesis only the $\beta\alpha$ and βp channels are considered as they are the only ones to have been observed, directly or indirectly [24]. For the β transition for the $\beta\alpha$ channel, the resonant state is illustrated in Figure 1.5(a), where the ground state of ${}^{11}\text{Be}$ ($1/2^+$) β decays to an excited state of ${}^{11}\text{Be}$ ($3/2^+$). This implies an angular momentum change of 1, a Gamow-Teller transition. The nature of the spin sequence of the βp channel isn't known as depicted in Figure 1.5(b); however, the transition is also assumed to be Gamow-Teller as discussed later in chapter 4.

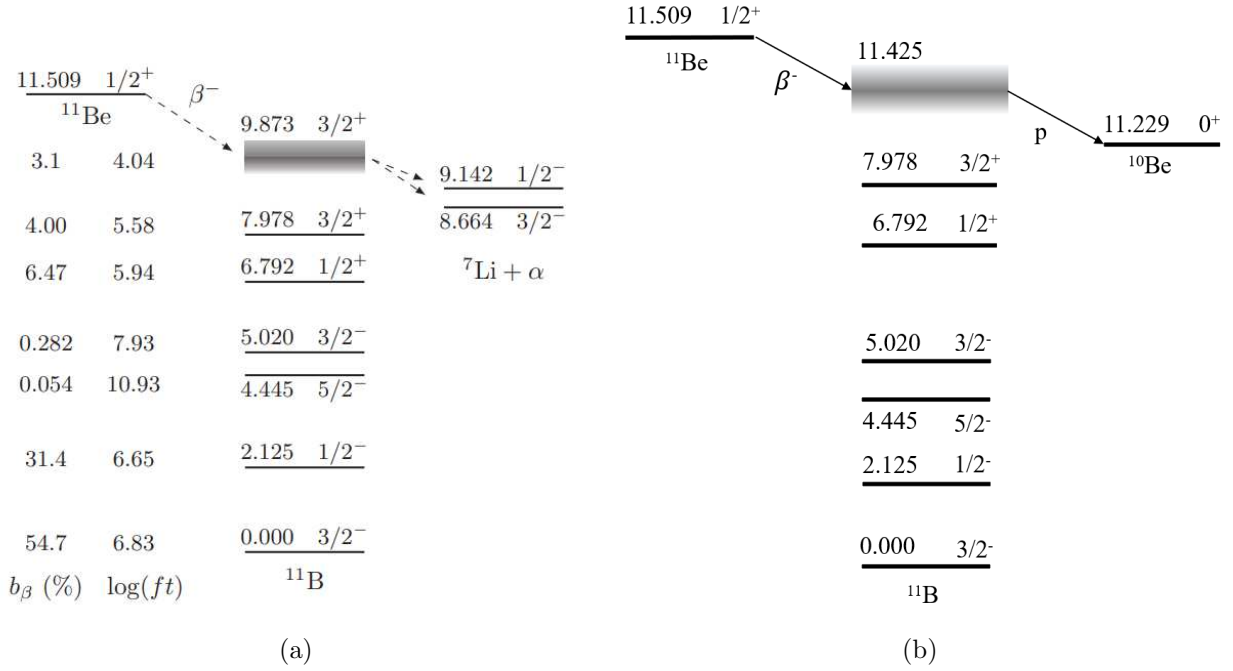


Figure 1.5: (a.) ^{11}Be decay scheme including the $\beta\alpha$ channel adopted from ref [21] (b.) ^{11}Be decay scheme including the βp channel [22]

1.3 Decay Rate Equation

As discussed earlier in the chapter, an important aspect to any radioactive decay process is the transition rate. The transition rate for β -delayed particle emission was thoroughly developed in ref [1]. Equations 1.13, 1.14 and 1.15 represent the decay rate of β -delayed particle emission [1].

$$d^7\Gamma \propto F_{\mp}(Z, E)(E_0 - E)^2 p E \times (g_1(E) + g_2(E)) \frac{\vec{p}}{E} \cdot \hat{k} + \frac{1}{10} \tau_{J', J''}(L) T^{(2)}(\hat{n}) : g_{12}(E) [\vec{p}/E, \hat{k}] dE d\Omega_e d\Omega_\nu d\Omega_n \quad (1.13)$$

$$\text{where } T^{(2)}(\hat{n}) : [a, b] = (\hat{n} \cdot a)(\hat{n} \cdot b) - \frac{1}{3} a \cdot b \quad (1.14)$$

$$\text{and } \tau_{J', J''}(L = 1) = \frac{2}{J'(J' + 1)} \begin{cases} (2J' + 3)(J' + 1) & J' = J'' + 1 \\ -(2J' + 3)(2J' - 1) & J' = J'' \\ (2J' - 1)J' & J' = J'' - 1 \end{cases} \quad (1.15)$$

From Equation 1.13, F_{\mp} is the Fermi function, E is the energy of the electron, p is the momentum of the electron and E_0 is the maximum value of E for a given excitation energy of the emitter, ^{11}B . To briefly cover this relationship, the energy levels relevant to the exotic decay channels of ^{11}B are distributions, meaning potentially there are many possible excitation energies. The Q-value is $m(^{11}\text{Be}) - m(^{11}\text{B}^*) = m(^{11}\text{Be}) - (m(^{11}\text{B}) + \text{Ex})$, where Ex is the excitation energy of ^{11}B . The maximum kinetic energy of the electron is the Q-value, implying that for each excitation energy there is a different maximum total energy of the electron.

The most interesting terms of Equation 1.13 incorporate spectral functions: g_1 , g_2 and g_{12} . From ref [1], regardless if the transition is purely a Fermi or Gamow-Teller transition, g_1 is simply 1. The g_2 term incorporates the correlation between the electron and neutrino with the factor $\vec{p} \cdot \hat{k} / E$, where \vec{p} is the 3-momentum of the electron and \hat{k} is the unit direction of the neutrino. The last term, g_{12} , includes $T^2(\hat{n})$, Equation 1.14, which represents a triple correlation between the electron (a), neutrino (b) and α particle (n). Lastly, $\tau_{J',J''}$ is a coefficient dependent on the spin sequence where J' and J'' are the spins of the emitter and daughter, respectively. For the $\beta\alpha$ decay channel, Figure 1.5, $J = 1/2$, $J' = 3/2$ and J'' is either $3/2$ or $1/2$ depending on whether the lithium atom is excited or in its ground state. In comparison to ref [1] it is fairly obvious that some terms are missing. A deeper discussion and example of a spectral function from ref [1] is given in Appendix C.

1.4 Previous Measurements of the βp channel of ^{11}Be

There are conflicting measurements of the branching ratio of the βp channel. In an effort to discover why the branching ratio of ^{11}Be is orders of magnitude higher than expected, the authors of ref [24] sought to measure the βp channel directly by measuring the emitted particle, the proton. Ref [24] claims through this direct observation the branching ratio is $1.3(3) \times 10^{-5}$, whereas Ref [13] claims through an indirect measurement a branching ratio of $8.4(6) \times 10^{-6}$. The difference between these two measurements is nearly a factor of two, which warrants discussion. Figure 1.6 depicts the energy distribution of the proton from the

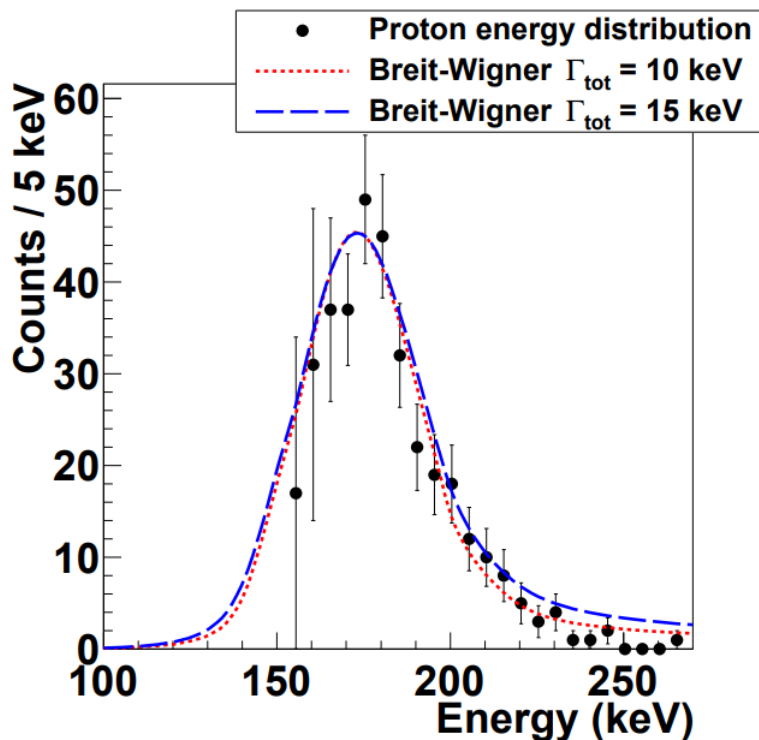


Figure 1.6: Energy distribution of β -delayed protons compared to a Breit-Wigner distribution. Adopted from ref [24]

βp channel from ref [24].

Much of the criticism levied against the direct measurement experiment stems from particle identification as the experiment was performed with the prototype Active Target Time Projection Chamber (pAT-TPC) [24]. This manner of detection does not differentiate the charged particle being detected, meaning the distribution, Figure 1.6, could include particles from the $\beta\alpha$ channel if the resonant states for the $\beta\alpha$ and βp overlapped. In contrast, the experiment described in the proposal, ref [3], from which this thesis is based on uses double-coincidence measurements for a ToF difference to identify the different β -delayed channels. This mitigates much of the possibility of misidentification from different β -delayed channels, however, not entirely. Chapter 3 and 4 give a deeper discussion of the potential background coincidences. To mention briefly, a recent paper has been published, ref [25] from the same group who performed the indirect measurement of the βp branching

ratio, and they determined the branching ratio to have an upper limit of 2.2×10^{-6} , after accounting for potential systematics not investigated in the previous measurement. For the purposes of this thesis, the branching ratio is assumed to be $8.4(6) \times 10^{-6}$ as determined by ref [13].

One final point requires some attention, the measured ft value for the βp channel has been quoted in ref [24] as 2.8(4), implying the transition is faster than so-called "super allowed" transitions. If correct, the small ft value means the decay must either be a Fermi or Gamow-Teller transition with a spin and parity of the resonance state being either $1/2^+$ or $3/2^+$, respectively. Additionally, the magnitude of the ft value implies the decaying neutron wavefunction in ^{11}Be and the populated proton wavefunction in ^{11}B must be very similar, and because ^{11}Be is a halo nucleus it is assumed the halo neutron is decaying. As the measurements in ref [24] have come into question, further information on this system is required.

CHAPTER 2

ION TRAPS AND THE DETECTION OF LOW ENERGY NUCLEAR RECOILS

The difficulty in the accurate reconstruction of the kinematics of a β decay lies with the detection of low energy recoils. The linear Paul trap has been successful in detecting low-energy recoils from the β decay of ^{134}Sb [26] and the β -delayed decay of other nuclei, notably ^{137}I [27]. The linear Paul trap confines an ion cloud using a radiofrequency field (RF field) and is advantageous as it eliminates much of the background resulting from source-scattering effects [26, 28, 29]. As a result, a new linear Paul trap called the BeTrap is being constructed to study the β -delayed particle emission of ^{11}Be .

2.1 Ion trap techniques

Ion traps can be categorized into electrostatic traps, electric radiofrequency traps and Penning traps [28]. A Penning trap confines ions using a static electric field and a strong magnetic field [30]. The electric field functions to confine the ion motion along the axis of the trap, while the magnetic field, parallel to the axis, confines the motion perpendicular to the trap axis [30]. However, a severe limitation to detecting low-energy recoils in Penning traps results from the magnetic field, which could adversely affect the detectors and trajectories of the ions. Furthermore, Penning traps also typically use a large solenoid coil to produce the magnetic field which does not allow optical access to the center of the trap, limiting the ability to monitor the decay radiation. By contrast, linear Paul traps do not utilize a magnetic field, meaning there is not the same potential adverse effects. Furthermore, the linear Paul trap also has an open geometry, allowing for the detectors to be brought close to the center of the trap.

RF Paul traps require the ions of interest to be nearly at rest. This process first requires deceleration to ≈ 100 eV [3, 28]. The ions are then placed in an RF-multipole structure which is typically constructed to produce a quadrupole electric field which confines the ions. Axial

confinement is provided by a DC electric field in the axial direction to generate a potential well to collect the ions in the center of the trap, as illustrated in Figure 2.1 [28, 31]. The injected ions are thermalized in the buffer gas and guided towards the trapping region at the end of the device [32]. Then to release the ion bunch, the voltage at the end of the device is pulsed down to open the trap [32]. Due to the typical use of segmented rods, this type of trap is referred to as a linear Paul trap. The physics will be discussed in greater detail in the next subsection.

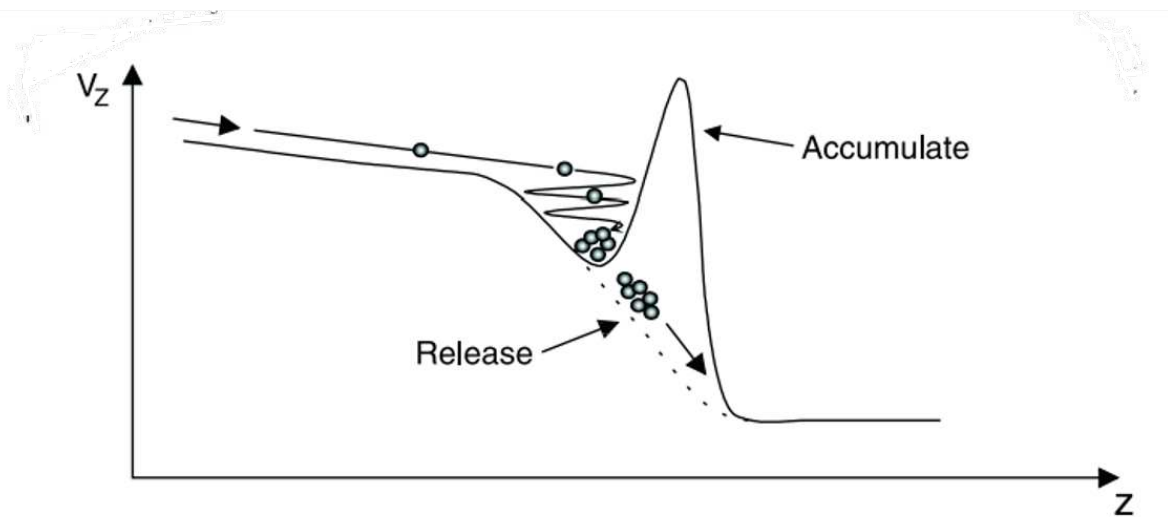


Figure 2.1: Potential well of RF-quadrupole ion trap where the curve is the axial potential and the dots represent ions. The gradient of the axial potential guides the ions to the end of the device where they are trapped in a potential well. To release the ions, the voltage is pulsed down. Adopted from ref [32].

To better confine and improve the properties of the ion cloud, the space between the rods is filled with a dilute gas, in this case He buffer gas, at a pressure of $\approx 10^{-5}$ Torr [3, 28]. The average loss or gain in ion kinetic energy is dependent on the relative mass of the ion and buffer gas atom under the action of the RF field [33, 34]. The relative mass determines how much the collisions interrupt the micromotion or the fast motion derived from the trap's driving frequency [34]. This introduces a degree of randomness which is transferred to the secular motion or the micromotion remaining coherent with the RF field [34]. If $M_{ion} \gg M_{buffer}$ then the collisions only slightly deflect the ions. The cumulative

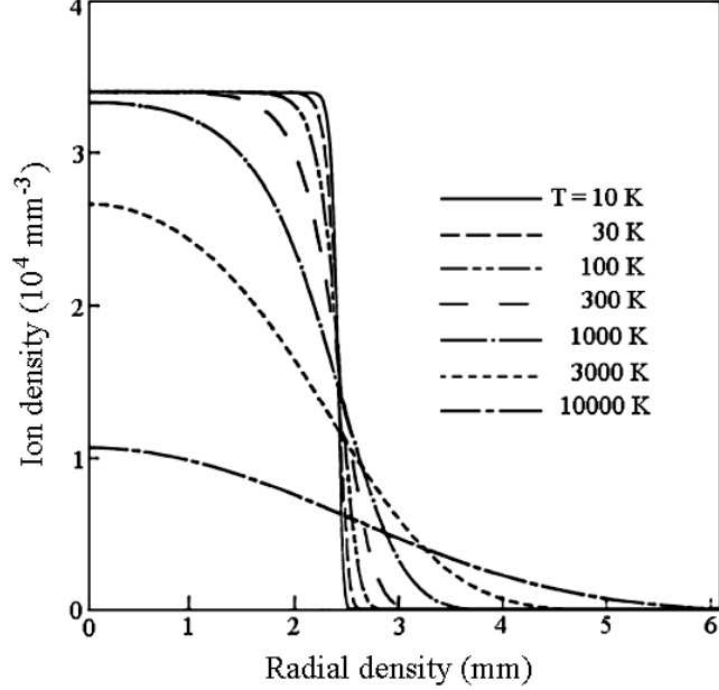


Figure 2.2: Radial density distribution in a Paul trap for different temperatures [34], adopted from [35]

result is the incremental draw of the kinetic energy from the ions' secular motion, which will on average cool the ions and lead to a higher concentration of the ion distribution about the center [34]. This implies more ions can be placed in the RF field at a higher density with less kinetic energy as a result of the buffer gas.

The higher concentration of ions is reflected in the number density or the number of ions per unit of volume, typically mm^3 [34, 35]. Figure 2.2 depicts the number density of a cloud ^{199}Hg when cooled by a He buffer gas to different temperatures [34, 35]. For context, the BeTrap experiment will be performed at room temperature; however, the cooling won't be sufficient to reach 300 K. The temperature of the ions in the trap should near 1000 K, and as depicted in Figure 2.2, the state resembles a Gaussian. Mirroring the shape at 1000K, the simulation uses a Gaussian for the ion cloud in the BeTrap, which will be discussed later in chapter 3.

2.2 Electromagnetic traps for charged particles

The defining feature of linear Paul traps is the confinement of ions without introducing scattering effects typically derived from the source being implanted in another material. To understand this confining phenomena physically, begin with a linear binding force [36].

$$F = -kr \quad (2.1)$$

From this linear binding force it is possible to derive the electric quadrupole field potential where r_0 is the radial distance from the center of a hyperbolic trap to ring electrode, Φ_0 is the potential difference between the ring and end caps and α , β and γ are constraints [34, 36, 37].

$$\Phi = \frac{\Phi_0}{2r_0^2}(\alpha x^2 + \beta y^2 + \gamma z^2) \quad (2.2)$$

However, Φ must obey Laplace condition with no free charge distribution [36]. Setting the constraints to resemble a potential produced by quadrupole electrodes, Equation 2.3 details the potential in cylindrical coordinates for a linear Paul trap where z_0 is the axial distance to the end cap [36, 37].

$$\Phi = \frac{\Phi_0}{r_0^2 + 2z_0^2} \text{ with } 2z_0^2 = r_0^2 \quad (2.3)$$

Figure 2.3 depicts the equipotential lines for a plane quadrupole field and the configuration of the hyperbolically shaped electrodes where the potential on each is $\pm\phi/2$ [36].

The configuration presented in Figure 2.3 will provide stability in two dimensions; however, due to repulsive force in the z direction, the particles will defocus [36]. This can be avoided by rotating the field so the focusing and defocusing will happen alternatively in each direction [36, 37]. This oscillation is the periodic applied voltage represented in Equation 2.4, where U is a DC voltage, V is the RF voltage and ω is the driving frequency [36].

$$\Phi_0 = U + V \cos \omega t \quad (2.4)$$

Mechanically, this can be visualized by a saddle shaped surface, Figure 2.4. The ball is analogous to an ion, and with adequate rotation of the surface the ion can be trapped by the

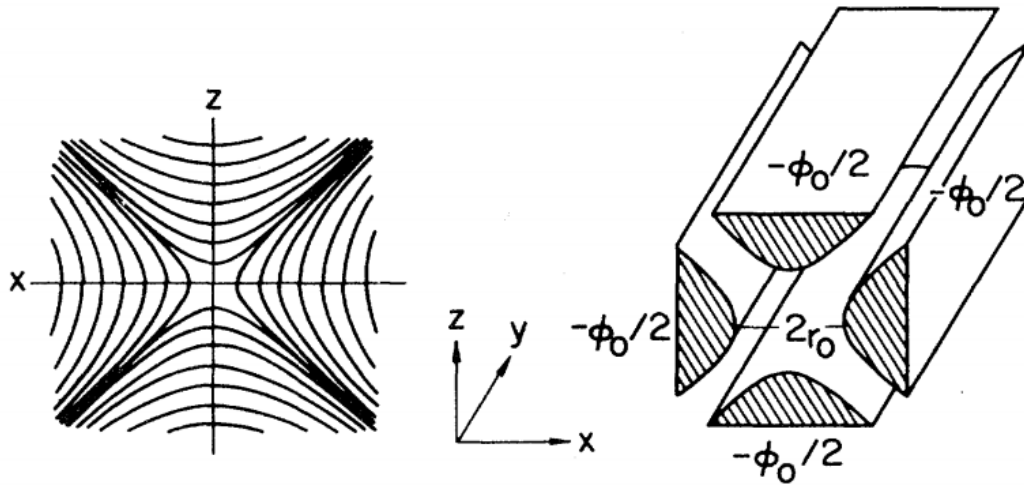


Figure 2.3: Equipotential lines (left) for the electrode configuration (right), adopted from ref [36]

potential [36, 37]. For information on the linear Paul trap's reduction of the second order Doppler effect, see Appendix D.

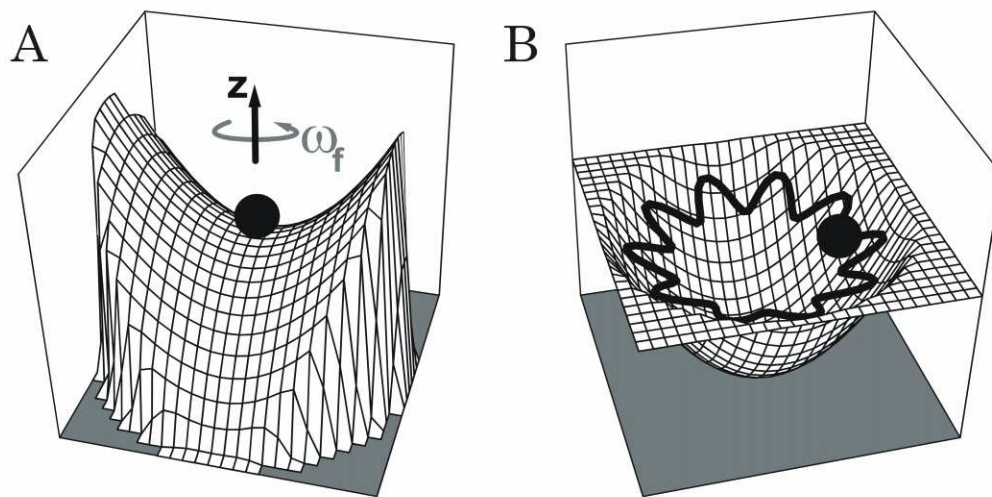


Figure 2.4: (A.) the ball is at the saddle point with one direction focused and the other defocused (B.) resulting pseudopotential and the trajectory of the ball. Figure adopted from ref [37, 38]

2.3 BeTrap

As mentioned previously, due to the success of linear Paul traps in the detection of low energy recoils, a new trap called the BeTrap is being constructed to study the β -delayed proton emission of ^{11}Be . BeTrap will have split cylindrical rods of 1/8 inch diameter, a distance of 12 mm from the center of the trap [3]. The RF field from the quadrupole structure will generate an electric field of $\approx 200 V_{pp}$ at a frequency of 1 MHz [3]. Figure 2.5 depicts a cut-away view of the BeTrap. The ion trap will have 3 Z-stack 97 mm by 79 mm MCP detectors to detect the recoil and emitted particles, a Germanium detector to detect γ rays and a ΔE -E plastic scintillator to detect the β particles [3]. The front face of the MCPs will be ≈ 70 mm from the trap center and will subtend a solid angle of $\approx 10\%$ [3].

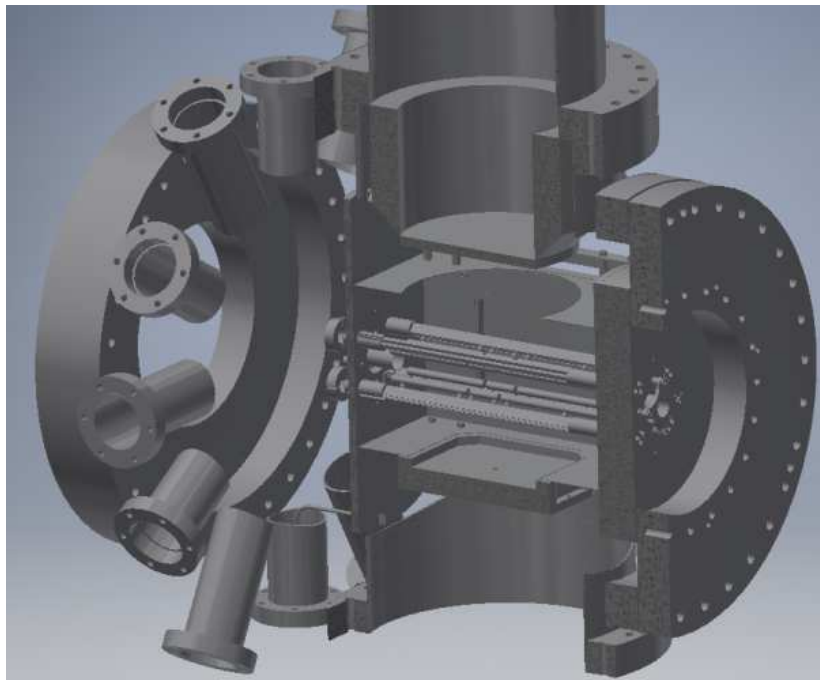


Figure 2.5: An Autodesk Fusion 360 cutaway model of the BeTrap, adopted from ref [3]

The most important feature of the BeTrap to the detection of the β -delayed channels of ^{11}Be are the MCPs. MCPs are made up from a dense stack of individual electron multiplier tubes and function as a fast high-gain amplifier [39, 40]. It is not only sensitive to electrons, but also to other charged particles and short wavelength electromagnetic radiation [40]. The

detection efficiency is generally dependent on the type and energy of the particle [40–42]. Figure 2.6 depicts the electron detection efficiency for MCPs between 3 keV and 2.6 MeV [41, 43]. Clearly, as the electron energy increases the efficiency decreases quite rapidly. This is relevant to the study of ^{11}Be as the random coincidences between the electron and the emitter, ^{11}B , must be accounted for in the simulations. This is discussed in greater detail in chapters 3 and 4.

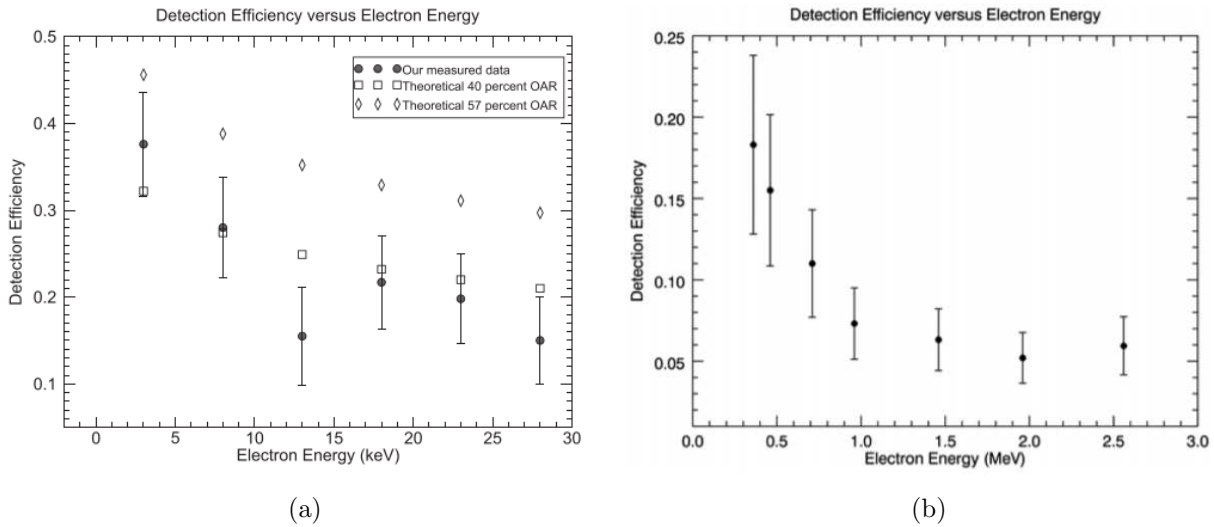


Figure 2.6: Adopted from [41, 43], MCP detection efficiency for electrons with energies between 3 keV to 2.6 MeV

Figure 2.6 illustrates why MCPs are valuable in the detection of the βp channel. Because the electrons will have energies on the order of an MeV, their detection using the MCPs will be relatively inefficient. This will reduce the number of random coincidences between the β particle and the low-energy recoils, and thereby suppress the background. In comparison, the MCP detection efficiency for ions from 0 keV to 4.75 keV, Figure 2.7, depicts a much greater efficiency [42]. As the ion energy increases, the absolute detection efficiency begins to flatten around 60% for energies greater than a couple of keV. The majority of the ions in both relevant β -delayed channels are much greater than 5 keV, and the lowest average energy nucleus, ^{10}Be , is measured at ≈ 18 keV. This relatively high detection efficiency is

valuable to the detection of the low-energy daughter nucleus, ^{10}Be , and the ToF difference measurements in general.

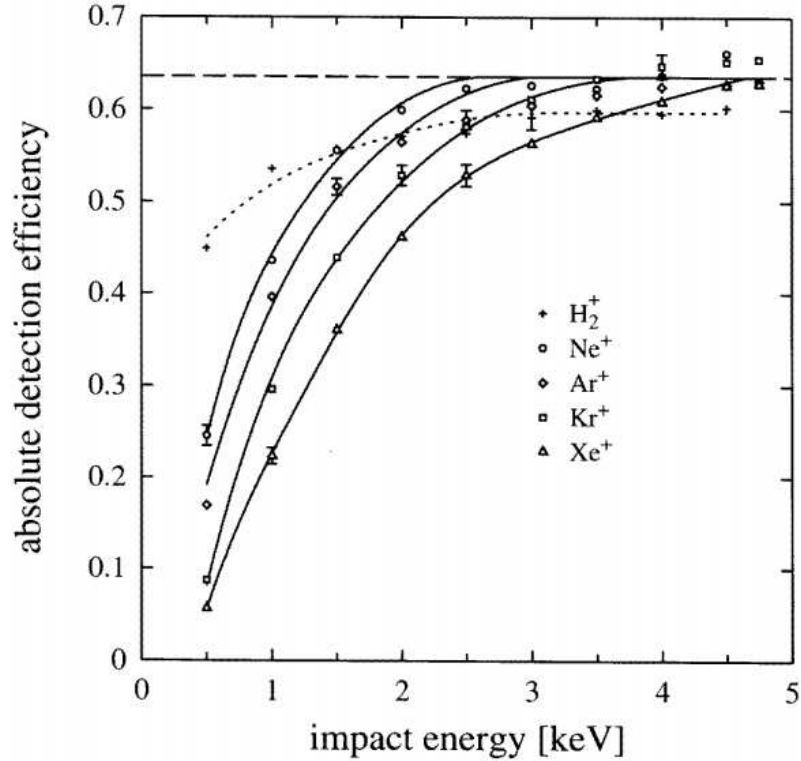


Figure 2.7: Adopted from [42], MCP detection efficiency for ions with energies between 0 keV and 4.75 keV

There are two additional detectors present in Figure 2.5, a $\Delta E - E$ scintillator and a Germanium detector. The $\Delta E - E$ scintillator is a combination of two scintillating detectors which function to identify charged particles. The $\Delta E - E$ technique functions by a particle with kinetic energy E_0 passing through the first detector and stopping in the second [44]. The partition of E_0 is different for different particles because of varying stopping powers [44]. Particles with the same kinetic energy have different profiles of energy deposition as a function of penetration depth, allowing for identification [44]. The $\Delta E - E$ scintillator functions within the experiment to monitor the β spectrum for the ^{11}Be decay. The Germanium detector is used for the high-resolution measurement of γ rays emitted in the decay.

CHAPTER 3

SIMULATION METHOD

GEANT 4 was the chosen simulation toolkit to simulate the particles in the linear Paul trap, BeTrap, described in the previous chapter. To provide the appropriate particle characteristics such as the 4-momentum and their direction as inputs into GEANT4, a rejection was implemented using the decay rate equation of β -delayed particle emission described in ref [1] and presented in chapter 1, Equation 1.13. The equation ensures triple correlation between the angles of the decay particles. The form of the equation presented in chapter 1 is a function of the electron energy and requires the momentum of the electron and the angles of the electron, neutrino and emitted particles (α and proton). Each of these values were simulated using randomization of the electron energy given an excitation energy of the emitter, ^{11}B , and conservation of momentum and energy to verify the characteristics of the neutrino and emitted particles.

3.1 GEANT4 and ROOT

GEANT4 is a toolkit which simulates the passage of particles through matter and is used for both full and fast Monte Carlo simulation of detectors in High Energy Physics [45]. A full simulation is the complete reconstruction of an event; a fast simulation is the use of parameterization to characterize the event [46]. GEANT4 allows the user to simulate particles in a particular environment, in this case, an ion trap depicted in the next subsection, Figure 3.1 and Figure 3.2. This portion of the simulation involving the complex geometry of the ion trap and the usage of GEANT4 in general was provided by Dr. Aaron Gallant.

ROOT is also a toolkit provided by CERN which functions to deal with big data processing, statistical analysis, visualisation and storage [47]. The TSpline3 class was implemented in several places and served to create a cubic spline from a 2 dimensional data set. The spline function would evaluate for a given input using piecewise third-order polynomials to

generate an output [48]. Furthermore, ROOT aided in both the visualization and verification of the results. In order to ensure the program was running correctly, ROOT was used to output the histograms relevant to the simulations such as the electron and neutrino energies. Lastly, in order to determine the effect of a varying cloud size in the ion trap, as depicted in the next chapter, a Gaussian distribution was fitted to the data using ROOT.

3.1.1 Geometry and Visualization of the Ion Trap

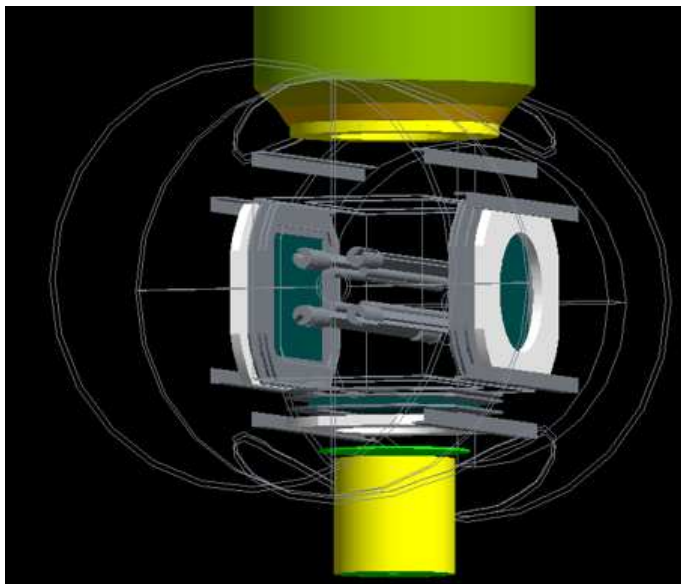


Figure 3.1: Simulated visualization of the ion trap using GEANT4

Figure 3.1 depicts a visualization of the ion trap created using GEANT4. From top to bottom, the large green cylinder is a $\Delta E - E$ plastic scintillator detector. The gray stands between the interior of the trap and the plastic scintillator are vacuum support structures. The blue squares are representations of the MCPs. The most interior rods are RF rods which have a frequency around 1 MHz and a peak-to-peak amplitude of ± 200 V. Lastly, the bottom-most yellow cylinder is a Germanium detector. All of the detectors were included in the GEANT4 simulation for completeness, as they are important for future experimental studies. In this thesis, the concern is the ToF differences between the "Left" and "Right" back-to-back MCP pair.

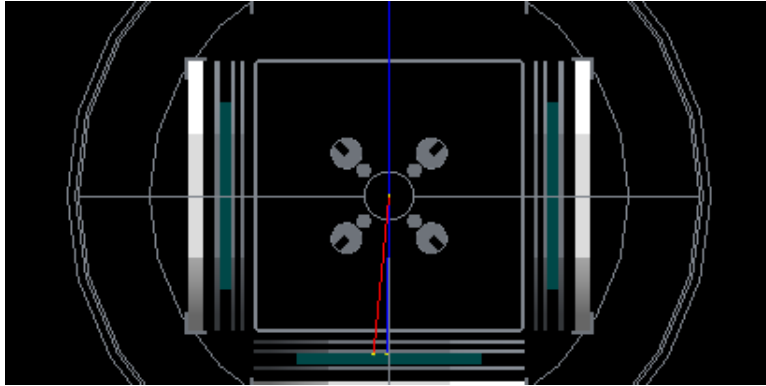


Figure 3.2: Simulated visualization of the ion trap using GEANT4

Figure 3.2 depicts three outgoing lines or visual representations of the resulting particles of the $\beta\alpha$ channel. The red represents negatively charged particles, in this case an electron. The blue represents positively charged particles, in this case the α particle and the ${}^7\text{Li}$ atom.

The RF potential is not taken into account when simulating the ToF differences, as the potentials are applied in such a way that the field on axis towards any of the MCPs is zero. However, consider a case where an α particle travels near an RF rod. The electric potential energy can be calculated from $U_E = qV$, where q is the charge and V is the potential. The RF rod has a potential of 200 V and the α particle has a charge of +2, meaning the potential energy is approximately 0.400 keV or $5.2 \times 10^{-4}\%$ of the α -particle's 770 keV kinetic energy. This effect changes the ToF of the α particle by $2.6 \times 10^{-2}\%$. For a lower energy particle, consider the daughter nucleus, ${}^{10}\text{Be}$, with a kinetic energy of 18keV and a charge of +1. ${}^{10}\text{Be}$ has an opposing potential energy from the RF rod of 0.20 keV or 1.1% of the proton's kinetic energy. So, for an average ${}^{10}\text{Be}$ atom the effect on the energy is $\approx 1\%$ for the worst case scenario. On average, it will be much smaller than this, meaning the effect can safely be ignored.

3.1.2 Detection Efficiency

As mentioned in chapter 2, the detection efficiency for MCP detectors for ions is roughly 60% [42]. The simulation uses a constant 60% detection efficiency for the heavy ions. How-

ever, for β particles the detection efficiency mirrors Figure 2.6, meaning the efficiency roughly decreases exponentially as the energy of the β particle increases. Figure 3.3 depicts an analytical model fit to the absolute detection efficiency data depicted in Figure 2.6 [3]. As depicted later in the chapter, Figure 3.8(a), the average energy of an electron will be on the order of an MeV, meaning the efficiency will be less than 10%. This, in combination with the kinematic cuts discussed in the next chapter, significantly reduces the number of random coincidences.

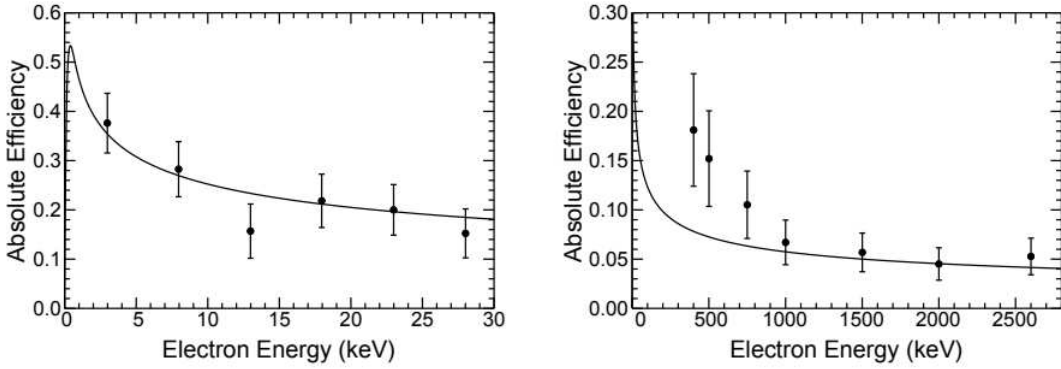


Figure 3.3: Absolute detection efficiency of β particles ranging from 3 keV to 2.6 MeV [41, 43]. Solid line is an analytical model fit to the data [3]. Adopted from ref [3].

3.2 Decay Rate Equation

In order to correctly parameterize the necessary decay particles for the GEANT4 simulation, the decay rate equation from ref [1] was implemented as a rejection test that would ensure the triple correlation between the β particle, neutrino and emitted particle. The decay rate equation takes inputs of the β particle, neutrino, emitted particle and the spin sequence of the decay. The following is Equation 1.13:

$$d^7\Gamma \propto F_{\mp}(Z, E)(E_0 - E)^2 p E \times (g_1(E) + g_2(E) \frac{\vec{p}}{E} \cdot \hat{k} + \frac{1}{10} \tau_{J', J''}(L) T^{(2)}(\hat{n}) : g_{12}(E) [\vec{p}/E, \hat{k}]) dE d\Omega_e d\Omega_\nu d\Omega_n.$$

Equation 1.13 takes this reduced form where only the leading order terms have been retained from the assumption $E/M \ll 1$, where E is the energy of the electron and M is the mass of the precursor, ^{11}Be . For the $\beta\alpha$ channel the maximum energy of the electron is the Q-value for the beta decay, 2.85 MeV, while the mass of ^{11}Be is 10266.6 MeV, meaning the terms proportional to E/M contributes approximately at the 0.028% level. This is much smaller than the expected precision of 1-5% for the measurement, thus these terms can be safely ignored.

3.2.1 Decay Rate Maximum

In order to determine whether a simulation event is accepted, a rejection test was implemented using the maximum value of the decay rate as a function of the excitation energy of the emitter, ^{11}B . To do this, the maximum of the differential decay rate was determined for each excitation energy. The rejection test functioned within this context by randomly generating a number $[0, 2\Gamma_{max}]$. The decay rate maximum is multiplied by a factor of two because in looking at Equation 1.13, the decay rate maximum occurs when the combination of the $g_1(E)$ term and the $g_2(E)\vec{p}\cdot\hat{k}/E$ term is $4/3$. The term involving the spectral function $g_{12}(E)$ can be ignored for this analysis as it only contributes a couple of percent as is shown in the next subsection. The $g_1(E)$ term will always be 1 for either a pure Fermi or Gamow-Teller transition. Assuming the β transition to be Gamow-Teller for both exotic channels, $g_2(E) = -1/3$. For the angular correlation factor, $\vec{p}\cdot\hat{k}/E$, the ratio of \vec{p}/E is assumed to be approximately 1, meaning the maximum occurs when $\vec{p}\cdot\hat{k}/E$ is -1. This results in the combination of terms involving $g_1(E)$ and $g_2(E)$ being $4/3$. However, to be conservative and to ensure the decay rate maximum is bounded in the rejection test, the maximum is multiplied by a factor of 2.

3.2.2 β - ν Correlation

The angular correlation between the β particle and the neutrino is the evaluation of the normalized dot product between the two particles and is important in verifying the results

of the decay rate. Additionally, because the change in the correlation from including or excluding the term is nominal, the term involving the g_{12} spectral function can be safely ignored in calculating the maximum value of the decay rate for a given excitation energy. Figure 3.4 shows this simulated angular correlation for accepted events.

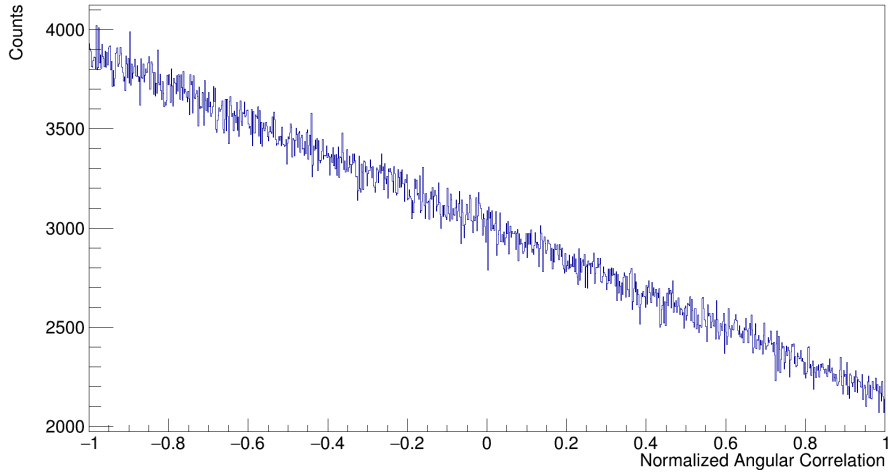


Figure 3.4: Simulated Distribution of $\hat{p} \cdot \hat{k}$ for a Gamow-Teller transition

Figure 3.4 was simulated by determining the dot product between the unit directions of the β particle and neutrino for accepted events. The particles' directions were randomized in accordance to a unit sphere, meaning the distribution of the dot product would be a straight line if not otherwise influenced. The distribution is a product of the $g_2(\vec{p} \cdot \hat{k}/E)$ term and displays a linear slope indicative of the g_2 spectral function. For a Gamow-Teller transition, g_2 is $-1/3$ which functions to influence the probability of accepting an event. If the β particle and neutrino are anti-parallel, the probability that event will be accepted is greater than if parallel as is depicted in Figure 3.4 at -1 and 1 , respectively. The overall effect of the factor g_2 is a slope in the angular correlation between the electron and neutrino.

The slope depicted in Figure 3.4 is approximately -865.252 ; however, in order to properly normalize, the slope must be divided by the central value or the y-intercept, 3016.6 . This produces a normalized slope of approximately $-0.287(1)$ which is close to the expected value of $-1/3$ arising from the $g_2(\vec{p} \cdot \hat{k}/E)$ term. When the g_{12} is set to zero, the slope of the distribution

is -0.286 or a 0.184% change. Because the difference is so nominal, for calculations of the decay rate maximum, it can safely be ignored.

The angular correlation is not precisely -1/3 because the ratio \vec{p}/E is not exactly 1. Equation 3.1 depicts an alternate version of \vec{p}/E , using natural units.

$$\frac{|\vec{p}|}{E} = \frac{\sqrt{E^2 - m^2}}{E} = \sqrt{1 - \frac{m^2}{E^2}} \quad (3.1)$$

Equation 3.1 approaches 1 when $E^2 \gg m^2$. As depicted in the simulated distribution of the electron energy for the $\beta\alpha$ channel, Figure 3.8(a), the most probable kinetic energy from that spectrum is approximately 1 MeV, and the rest mass of an electron is 0.511 MeV. The ratio m^2/E^2 is therefore roughly $(0.25)^2$, meaning the $g_2(\vec{p}\cdot\hat{k}/E)$ term from this calculation is approximately -0.287, which is in perfect agreement with the value determined in Figure 3.4.

3.2.3 Fermi Function

The coefficient $F_{\mp}(Z, E)$ is the Fermi function, as previously discussed in chapter 1. The Fermi function used within the simulations was derived from the data sheets in ref [10]. Equation 1.11 is a reasonable approximation; however, the values in ref [10] are tabulated for specific cases, meaning less approximation and higher accuracy. To determine the Fermi value for an arbitrary electron momentum from the data sheets, a cubic spline function was implemented [10].

3.3 Initial Set-up and Variable Ion Cloud Size

The initial set-up of the simulation involves the initialization of the masses of the particles as well as the particles themselves. The particles were created with a struct containing properties such as their 4-vector momentum, position in the trap and kinetic energy. Each of the particle's directions were randomly distributed over the unit sphere.

The decay locations of the particles in the trap were randomized using a Gaussian distribution, as mentioned in the previous chapter. The FWHM of the ion cloud size was variable to characterize the ion trap. To determine the influence of the cloud size on the detected dis-

tribution of the difference in hit positions, the cloud size’s FWHM was incrementally changed by 0.5 mm ranging from 0.0 mm to 4.0 mm. The distribution was then fitted using ROOT, which would provide the parameters of the fit including the constant, mean and sigma and their corresponding errors. To ensure the fit was accurate, the standard deviation’s error was limited to less than 10% of the value.

To determine the parameters of the kinematic cut to suppress the background coincidences, the cloud size FWHM was set to 1.0 mm, the expected size of the cloud during experimentation. The same detected distribution of the difference in hit position was plotted in ROOT; however, the goal was the limitation of the background coincidences in an effort to preferentially select the β -delayed channels. Both the influence of the cloud size and the kinematic cut will be discussed in much greater detail in the next chapter.

3.4 Verification of the β , ν and α Energy Distributions

Each energy distribution was used as a form of verification which indicates whether the simulation was performing as expected. This subsection mirrors the structure of the code, setting up the excitation energy of the emitter and determining the resulting energies of the decay particles, namely the emitted particles. The subsection speaks primarily to the $\beta\alpha$ channel unless specified otherwise. All of the relevant βp channel energy distributions are in Appendix E.

3.4.1 Excitation of ^{11}B

For the $\beta\alpha$ case, the ground state of the precursor, ^{11}Be , β decays to an excited state of the emitter, ^{11}B . However, the excited state is not a discrete state, but rather a resonance centered at 9873 keV [21]. The excitation energy distribution was determined using R-Matrix theory with parameters experimentally determined in ref [21].

The phenomenological R matrix method is used in nuclear physics particularly for the analysis of low-energy scattering data [49]. The goal of the R matrix method is the parameterization of observed quantities, in this case the observed α and ^7Li spectrum [21, 49].

Figure 3.5(a) shows the observed energy and subsequent R matrix fit [21].

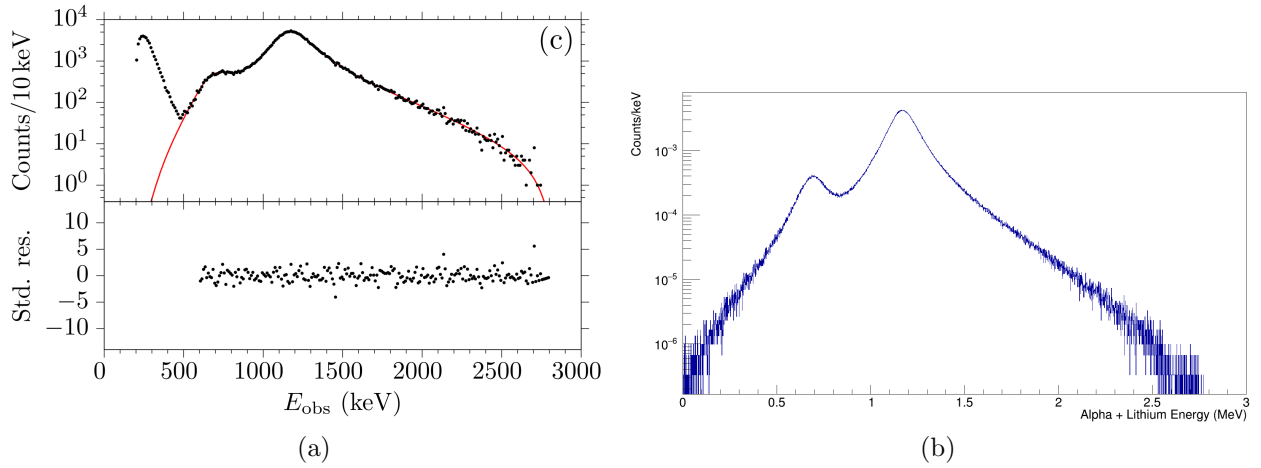


Figure 3.5: (a.) was adopted from ref [21], observed energy (black) and an R matrix fit (red) (b.) Simulated distribution of the kinetic energy of the α particle + lithium atom

The E_{obs} is the combination of the kinetic energy of the α particle and lithium atom as well as a broadening term. The broadening term stems from the Si detector's measurement of some of the β particle's energy, as well as the Si detectors not having perfect resolution [21]. To emulate the proper excitation energy which would result in the curve depicted in Figure 3.5(a), the same or close to the same parameters were used with slight deviations to account for the broadening. Figure 3.5(b) shows the simulated sum of the kinetic energy of the α -particle and the lithium atom. The two peaks in Figure 3.5(b) correspond to the excited and ground states of ${}^7\text{Li}$ with peaks at 0.731 MeV and 1.209 MeV above the $\beta\alpha$ channel Q-value, respectively. Figure 3.6 depicts the simulated excitation energy of the emitter for the $\beta\alpha$ channel resulting from the parameters developed using R-matrix theory.

For the βp case the physics and implementation is very similar. The excited state of ${}^{11}\text{B}$ relevant to the proton case is assumed, for simplicity, to be a Gaussian distribution centered at 11.425(20) MeV with a standard deviation of 12(5) keV [24]. The nature of the resonant state for the βp channel can be approximated, as the goal of the simulations is the verification of the differentiation of the ToF differences.

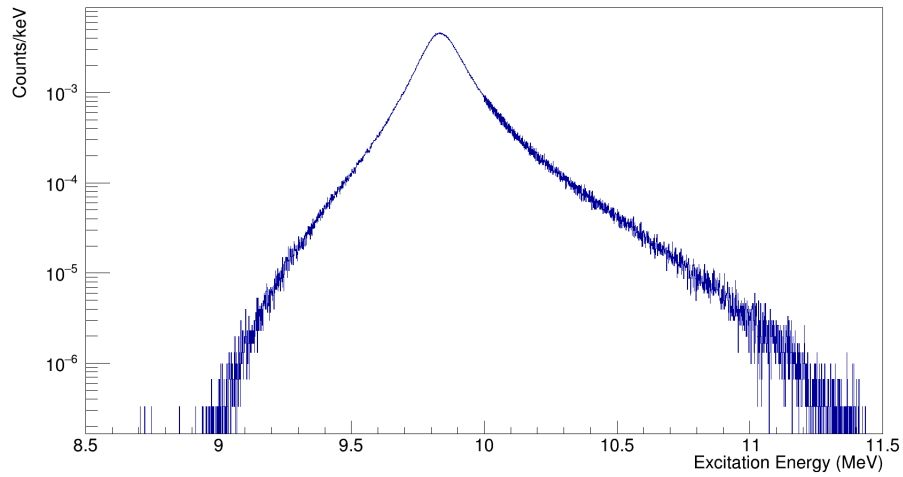


Figure 3.6: Simulated Distribution of ^{11}B Excitation Energy

3.4.2 β and ν Energy Distributions

The total energy of the electron can be deduced using the Q-value, or the differences in the sum of the masses of the initial reactants and the sum of the masses of the final products. The Q-value in this case also represents the total kinetic energy imparted to the electron and neutrino. Therefore, the maximum possible kinetic energy of the electron is the Q-value. The kinetic energy is randomized between $[0, Q]$. Figure 3.7 shows the simulated Q-value distribution for the $\beta\alpha$ channel.

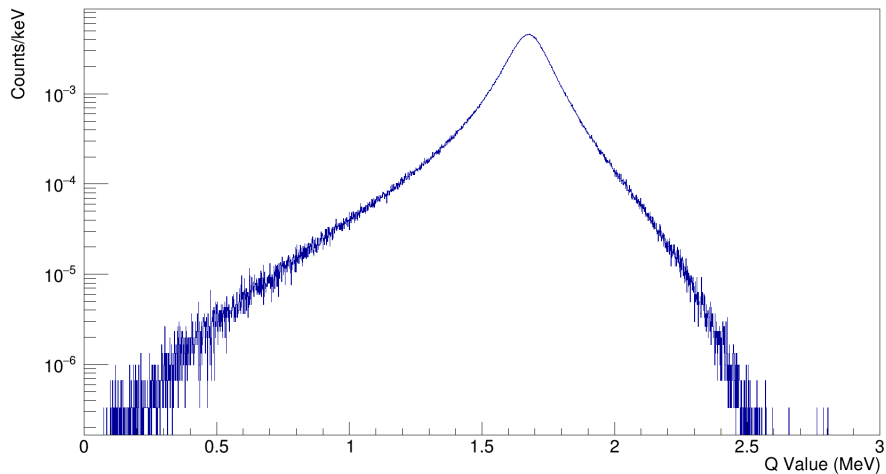


Figure 3.7: Simulated Distribution of Q-values for the $\beta\alpha$ decay channel

The Q-value depicted in Figure 3.7 is defined as $Q = m(^{11}\text{Be}) - m(^{11}\text{B}^*) = m(^{11}\text{Be}) - m(^{11}\text{B}) - \text{Ex}$. The histograms of the Q-value and excitation energy are mirror images with one being flipped about the y-axis. Physically, it could be conceptualized as the larger the excitation energy of ^{11}B , the smaller the differences between the masses, or the Q-value. Using the Q-value as the bounds of randomization for the β particle, Figure 3.8 shows the simulated total electron and neutrino energy distributions for the $\beta\alpha$ decay channel.

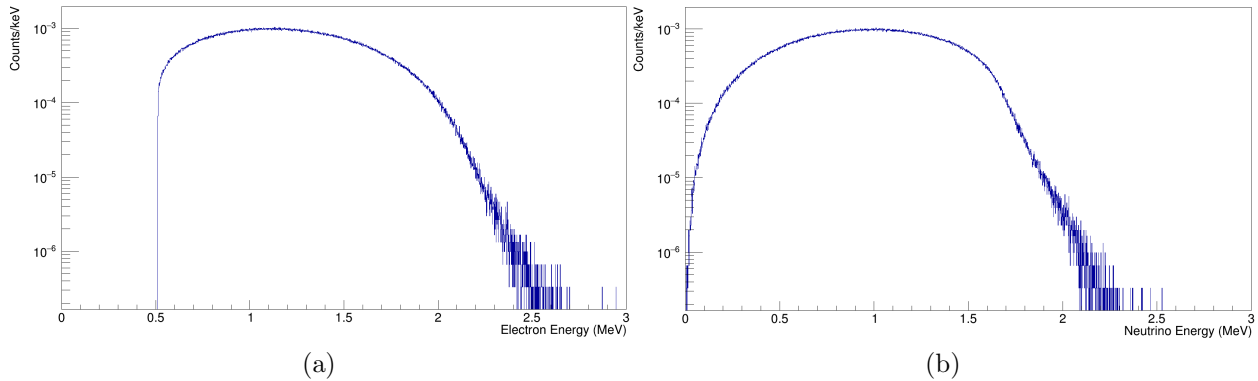


Figure 3.8: (a.) Simulated distribution of the total electron energies for the α decay channel
(b.) Simulated distribution of neutrino energies

The total energy of the electron must be in the range $[m_e, Q + m_e]$ or in the range of the rest mass to the rest mass plus the maximum kinetic energy of the electron which is depicted in Figure 3.8(a). Assuming the excitation energy of the emitter to be its minimum, approximately $\text{Ex} = 8664 \text{ keV}$, this would result in a Q-value of approximately 2.845 MeV [21]. This implies the total electron energy cannot exceed 3.356 MeV, which from Figure 3.8(a), the simulation does not.

In this analysis the neutrino is treated as massless, meaning $p_\nu = E_\nu$ in natural units. The conservation of energy limits the neutrino's maximum energy to be the Q-value. From our previous calculations, the maximum Q-value is approximately 2.845 MeV which is clearly not exceeded in Figure 3.8(b).

3.4.3 Emitted Particle Energy Distribution

In reference to both the $\beta\alpha$ and βp cases, using conservation of energy and momentum, the energy of the emitted particle is the following, Equation 1.12.

$$E_{emitted} = \frac{m_{precursor}^2 + m_{daughter}^2 - m_{emitter}^2}{2m_{precursor}}$$

In both cases for Equation 1.12, the precursor is ^{11}Be and the emitter is ^{11}B . The daughter atoms for the $\beta\alpha$ and βp cases are ^7Li and ^{10}Be , respectively.

3.4.4 Galilean Transformation

The previous calculation took place in the rest frame of the emitter. However, the decay rate equation requires all quantities to be in the rest frame of the precursor. A Galilean transformation translates the energy and momenta from the rest frame of the emitter to the rest frame of the precursor. Equation 3.2 demonstrates this Galilean transformation.

$$\vec{p}_{emitted} = -\vec{p}_{daughter} + \frac{m_{emitted}}{m_{emitter}}\vec{p}_{emitter} \quad (3.2)$$

Equation 3.2 is approximated as non-relativistic as the momentum of the emitter is relatively small or $\beta = v_{emitter}/c \ll 1$. In order to assume the emitter's momentum can be approximated as non-relativistic, the rest mass must be much greater than the kinetic energy or $\frac{1}{2}mv^2 \ll mc^2$. The rest mass for the emitter is on the order of a GeV, whereas the kinetic energy is less than a keV, allowing for the use of the non-relativistic calculation.

CHAPTER 4

SIMULATION RESULTS AND DISCUSSION

The majority of the previous chapter sought to validate the decay rate equation inputs such as the decay product's energy distributions compared to expectation. This chapter mirrors that approach for the final results of the simulation. The goals of the simulation were as follows:

- Verify the ToF difference profiles for the β , βp and $\beta\alpha$ decay channels
- Determine the parameters of a kinematic cut to suppress the random coincidences
- Determine the influence of the cloud size on the detected difference in hit position

The goal of determining the ToF difference profiles is the verification of the differentiation between the $\beta\alpha$, βp and β decay channels. Determining the parameters for a kinematic cut will function in experimentation to aid in the suppression of many of the random coincidences. Lastly, determining the influence of the cloud size on the detected distribution of the difference in hit positions will allow for a roundabout way of determining how well the ion trap is functioning during experimentation.

4.1 ToF Difference Profiles

The measurement and proper detection of low energy particles is difficult; however, with a specific type of ion trap it is possible as discussed in chapter 2. Another difficulty arises from the proper identification of a detected particle, and one way to differentiate the channels is through ToF difference profiles. When a particle hits the MCP, the metaphorical clock begins and once another particle hits then the clock stops. This difference in the ToFs between particles allows for the differentiation between decay channels.

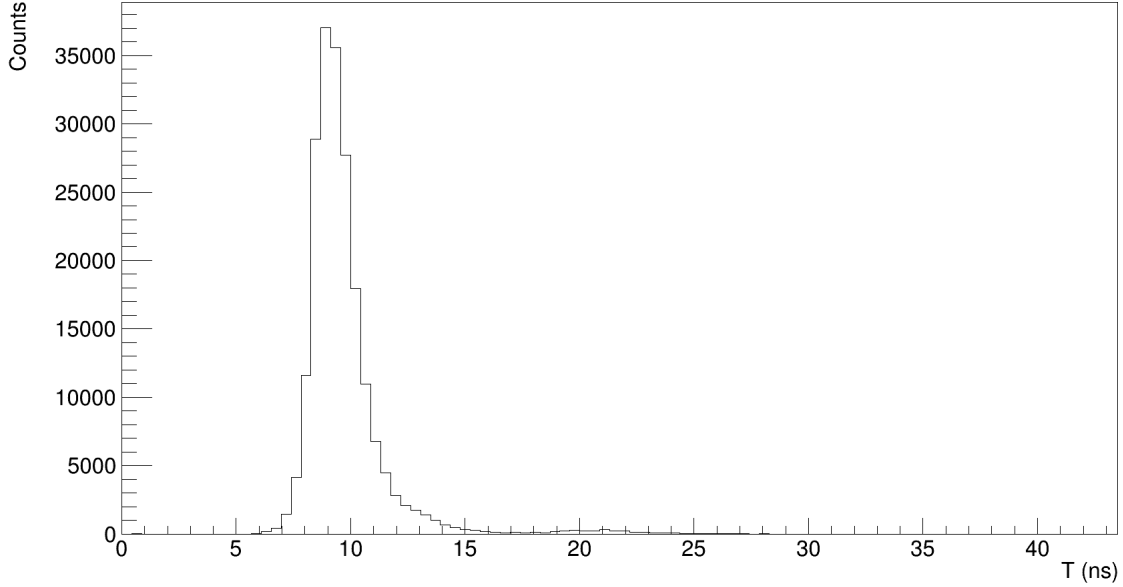


Figure 4.1: Simulated ToF of the $\beta\alpha$ channel

Figure 4.1 displays the simulated ToF for the $\beta\alpha$ decay channel. Figure 4.1 can be verified using the average kinetic energy of the α particle, 770 keV, and the lithium atom, 440 keV. Assuming non-relativistic calculations, the momenta are used to determine the velocities. From the dimensionality of the ion trap, the particles need to travel 70 mm from the center of the trap, meaning the resulting average ToFs for the α and lithium are 12 ns and 21 ns, respectively. The MCP will detect the α particle initially and after approximately 9 ns, the lithium will be detected. This difference in the ToFs is what is plotted in Figure 4.1. For more information on the ToF difference profile for the $\beta\alpha$ channel see Appendix F.

Figure 4.2 displays the simulated ToF difference profile for the βp decay channel. Similar to the calculation of the average ToF difference for the $\beta\alpha$ channel, the βp channel's average ToF difference can be calculated from the kinetic energies of the decay products, the proton (178 keV) and ^{10}Be atom (18 keV). This results in an average ToF of 12 ns and 119 ns for the proton and ^{10}Be atom, respectively, and a ToF difference of 107 ns. However, the mean ToF difference depicted in Figure 4.2, 114.5 ns, does not perfectly match as the calculation is an approximation which assumes the decay products have a perfect trajectory aimed at the

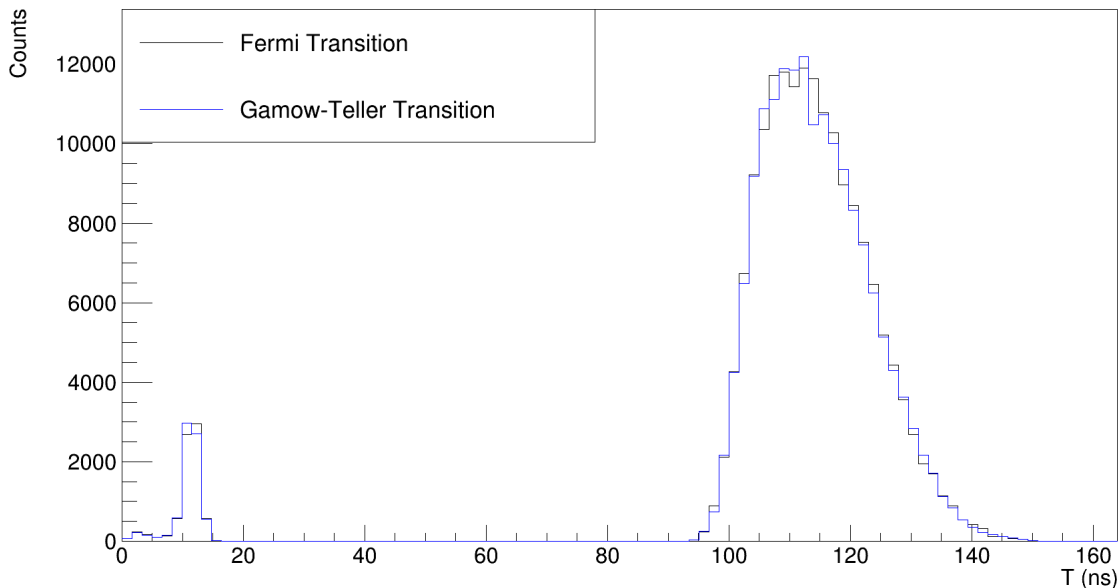


Figure 4.2: Simulated ToF of the βp channel

center. The difference between the approximated calculation and the simulations is 6.5%, well within reason.

In simulating the ToFs for the βp channel, there is inherent uncertainty whether the β transition is Fermi or Gamow-Teller. This results from a lack of knowledge about the emitter state's spin and parity. The assumption is the transition will be Gamow-Teller based on the parity and spin of the emitter state and the transition of the $\beta\alpha$ channel; however, this isn't a certainty until the experiment is carried out. Nevertheless, the profiles of the ToF differences for either a pure Fermi or a pure Gamow-Teller transition, Figure 4.2, are very similar as they share nearly the same mean ToF difference, 114.6 ns and 114.5 ns, respectively. Still, determining the transition is very important since there is some question of if this decay has ever actually been observed [50]. However, based on Figure 4.2, discerning whether the transition is Fermi or Gamow-Teller would be very difficult because of the similarities in profile.

Within Figure 4.2 a secondary peak near 12 ns is present, which defies the calculated and expected ToF difference for the βp channel. The secondary peak stems from electron-

proton coincidence. The β efficiency for the MCPs is relatively insignificant as depicted in Figure 2.6, but non-zero. The β particle has an average ToF of 0.12 ns, assuming an MeV of kinetic energy, meaning the ToF difference from an electron-proton coincidence would be approximately 12 ns which is in excellent agreement with the secondary peak in Figure 4.2.

The difference in the $\beta\alpha$ and βp ToF differences stems from the differentiation in excitation levels of ^{11}B . The $\beta\alpha$ channel imparts significantly more energy as the average kinetic energies of the daughter atom and emitted particle are significantly greater. As mentioned previously, the average kinetic energies of the α particle and ^7Li are 770 keV and 440 keV relative to the proton (178 keV) and ^{10}Be atom, respectively [18]. Because the energy imparted to the daughter nucleus for the βp is on the order of tens of keV compared to the roughly hundreds of keV imparted to the proton, the ToF difference is much greater.

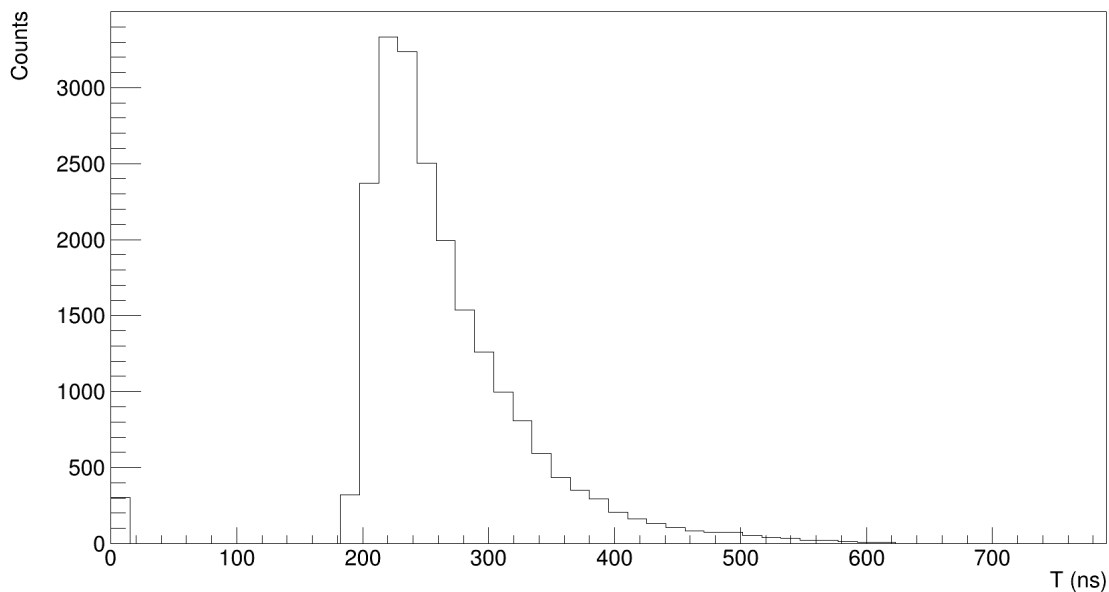


Figure 4.3: Simulated ToF of the β decay channel

Figure 4.3 depicts the simulated distribution of the β decay channel. The simulation of the β decay channel was provided by Dr. Aaron Gallant, as the complexity was out of the scope of this thesis. However, to speak briefly on Figure 4.3, the importance of the simulation of the β decay channels is the implementation of an energy cut. An energy cut

in this context refers to a minimum excitation energy of the emitter that must be exceeded for the event to be differentiated from the other decay channels. The lower the excitation energy of the emitter, the less kinetic energy imparted to the emitted particle and daughter atom, meaning the ToF difference could increase. If the ToF difference is great enough in either of the β -delayed channels, the decay channel could be misidentified. The likelihood of the $\beta\alpha$ channel having a ToF difference at or exceeding 190 ns, or the beginning of the ToF difference peak of the β decay channel, is unlikely as the ToFs of the emitted particle (α particle) and daughter atom (${}^7\text{Li}$) are very close, 12 ns and 21 ns, respectively. However, there is a great enough differentiation in the ToFs for the βp channel such that a cut energy must be considered. Assuming the ToF difference must reach or exceed ≈ 190 ns and the ratio of the kinetic energy of the emitted particle (proton) and daughter atom (${}^{10}\text{Be}$) remains the same, then the excitation energy of the emitter must exceed 11.291 MeV, a difference of 134.1 keV from the center of the resonance state, 11.425(20) MeV [24]. This would result in a lower limit of the kinetic energies of the ${}^{10}\text{Be}$ atom and proton being approximately 6 keV and 56 keV, respectively.

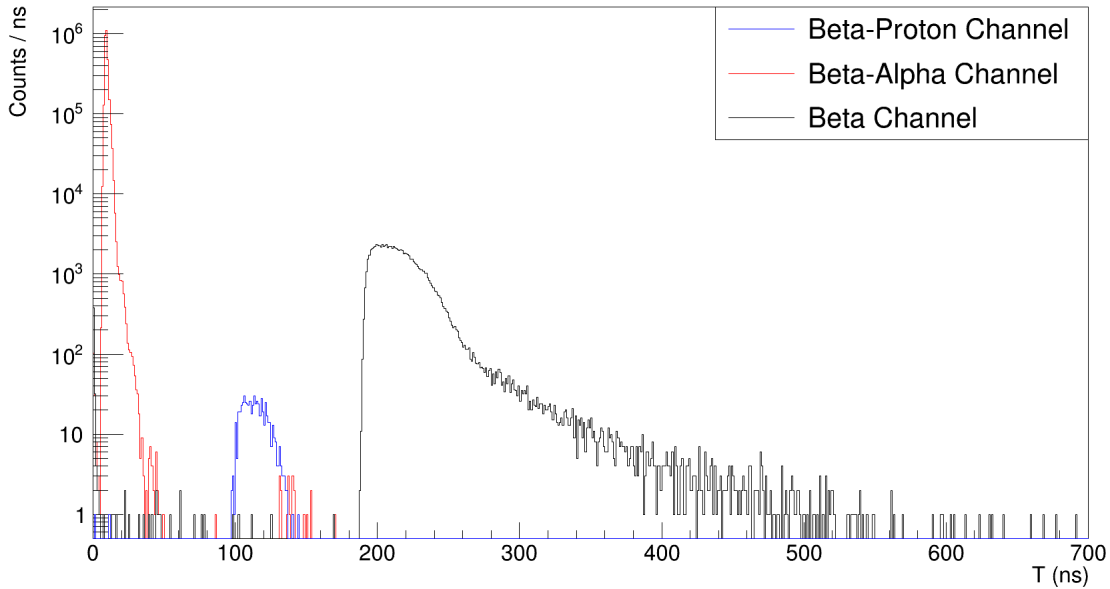


Figure 4.4: Simulated distribution for the $\beta\alpha$, βp and bound state β decay. Each channel was simulated with the literature branching ratio and includes the kinematic cuts

Lastly, Figure 4.4 depicts the ToF difference profiles for each simulated channel. Figure 4.4 is to the approximate scale of what is expected based on the branching ratios of each channel, MCP detection efficiency, geometric efficiency of the ion trap and the kinematic cut placed on the difference in hit positions distribution, ± 10 mm. The kinematic cut is discussed at length in the next subsection.

4.2 Kinematic Cuts

In preparation for experimentation, one of the ways to characterize the ion trap is a determination of the parameters of a kinematic cut needed for the spectra. A kinematic cut functions to suppress the background stemming from random particle coincidences by setting limits to the difference in hit positions. The daughter atom and emitted particle are assumed to be relatively back-to-back resulting from the conservation of the momentum. A kinematic cut that isolates those events can preferentially select the β -delayed channels and help suppress the background coincidences. Figure 4.5 depicts the back-to-back hit positions for the β -delayed channels. The difference in hit positions can be seen in Figure 4.5 as the difference between $Y_{Left} - Y_{Right}$. If the hit positions are back-to-back, this value will be near zero. Figure 4.6 depicts the detected difference in hit positions distribution for the β , βp and $\beta\alpha$ decay channels at a cloud size FWHM of 1.0 mm.

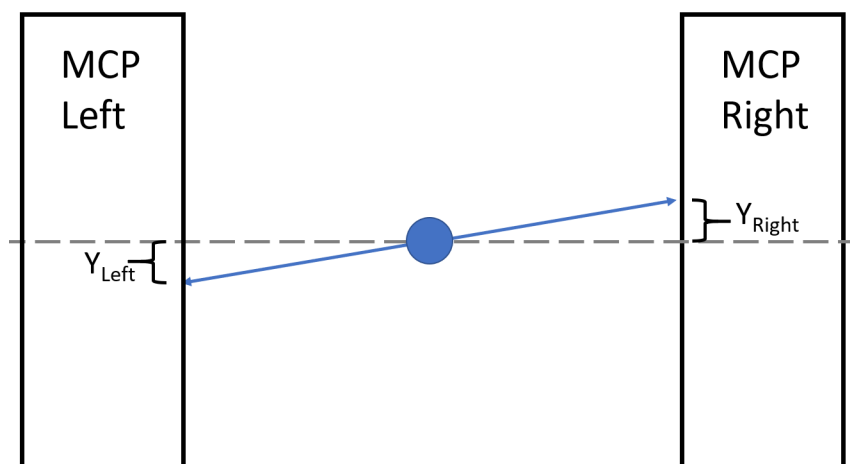


Figure 4.5: Cartoon illustrating a back-to-back detection

From Figure 4.6, the β decay channel, Figure 4.6(a) and Figure 4.6(b), depict the background. A purely random background would be a flat distribution; however, there is minor correlation between the β particle and the emitter, resulting in some curvature. For the β -delayed distributions, each distribution has a clear narrow peak centered at zero, indicative of back-to-back hits. Figure 4.6(c) through Figure 4.6(f) also have very widened bases or a relatively higher difference in hit positions, representing the background coincidences. From Figure 4.6, the kinematic cuts for the β -delayed channels should limit from -10 mm to 10 mm as to cut the background coincidences depicted with the wide base.

The importance of a kinematic cut is depicted in its suppression of the background, which can be approximated beginning with the rate of random coincidences. Assuming a realistic number of decays for the simulation, the activity of the ^{11}Be decay can be approximated at 5000 decays per second [3]. The geometric efficiency is assumed 9%, and from the detection efficiencies discussed in chapter 2, the β efficiency is 6% for energies on the order of an MeV and the ion efficiency, 60% [3]. This will result in approximate rates of 30 Hz and 270 Hz for the β particles and ions, respectively. The dark count, or the rate at which the MCPs will randomly fire, is 100 Hz from previous experimentation [3]. The random coincidence rate plus the dark count rate per detector is therefore ≈ 400 Hz. From Figure 4.2, the time interval covered by the βp channel is 60 ns; therefore, the probability of a random coincidence must be integrated over that time interval. Assuming both MCPs are identical, the coincidence rate within the time window is 0.02 Hz [3]. However, this coincidence rate is further reduced by a kinematic cut. After applying the kinematic cut determined for the β particle and slow recoils of approximately 5.5%, the random coincidence rate is 1×10^{-3} Hz [3]. In comparison, the expected βp rate is 2.6×10^{-3} Hz, 2.6 times larger than the random coincidence rate. The implementation of this kinematic cut would help in differentiating the βp channel by suppressing the background.

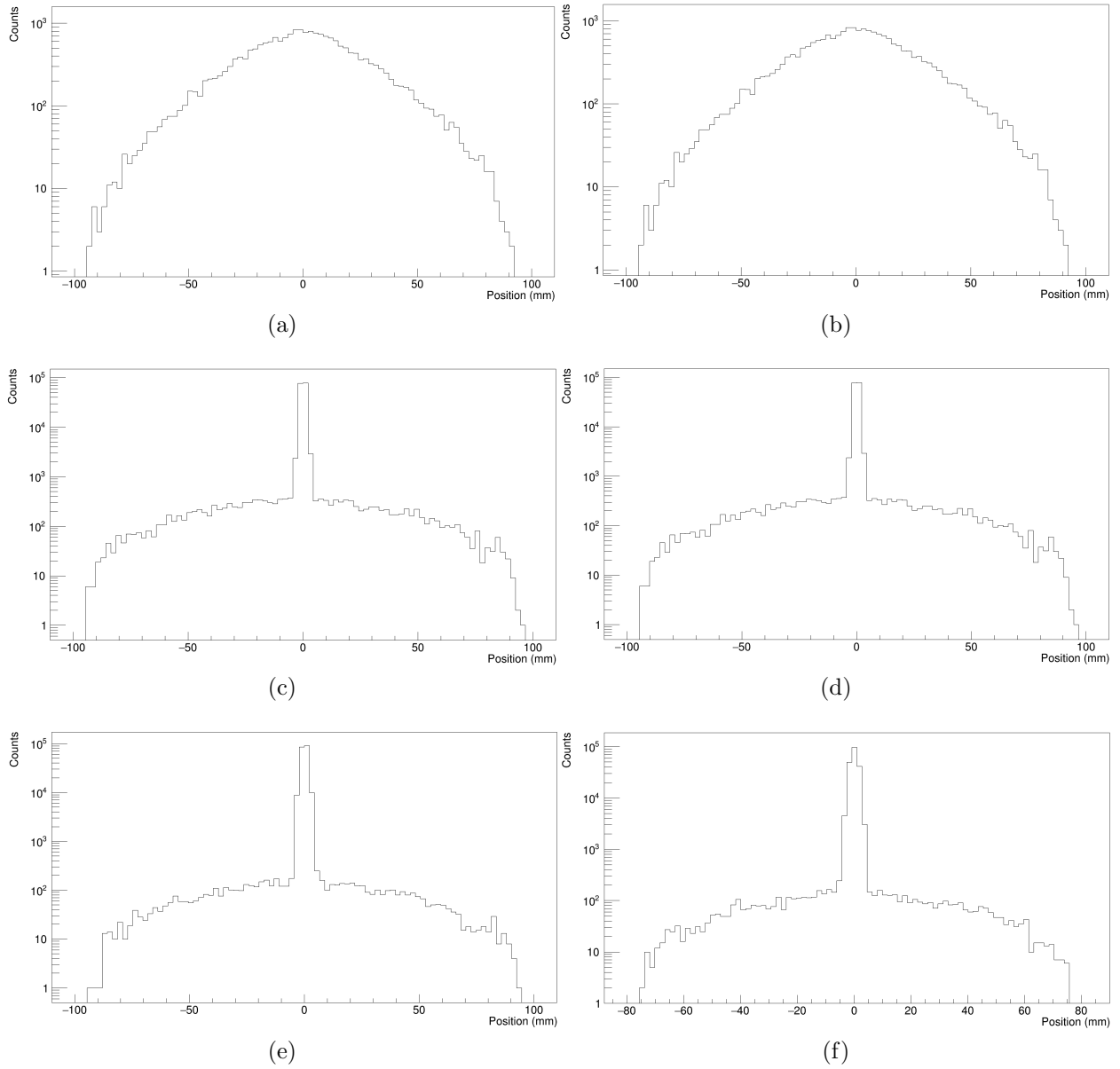


Figure 4.6: (a.) and (b.) Simulated detected difference in hit positions for β decays along the x axis (left) and y axis (right), (c.) and (d.) Simulated detected difference in hit positions for βp channel along the x axis (left) and y axis (right), (e.) and (f.) Simulated detected difference in hit positions for $\beta\alpha$ channel along the x axis (left) and y axis (right)

4.3 Cloud Size

One of the ways to characterize the simulated ion trap is an assessment of the relationship between the FWHM of the ion cloud and its corresponding affect on the detected difference in hit positions. In order to understand the influence of the cloud size, a Gaussian is fitted to the detected distribution of the difference in the hit positions. Figure 4.7 depicts an example of this Gaussian fit placed on the the difference in hit positions for the $\beta\alpha$ channel at a cloud size (FWHM) of 4.0 mm and the standard deviation of the Gaussian fit is 4.1(2) mm.

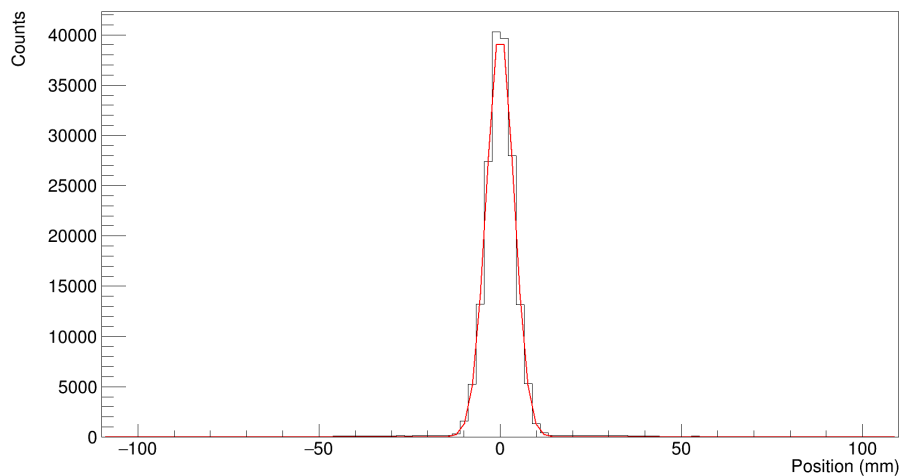


Figure 4.7: Simulated Distribution of the detected difference in hit positions for the $\beta\alpha$ channel at an ion cloud size of 4.0mm for the MCP detectors

Figure 4.8 depicts the relationship between the standard deviation of the Gaussian fit on the difference in hit positions for both the $\beta\alpha$ and βp decay channels for the MCP detectors along the x-axis and y-axis. Figure 4.8 suggests as the cloud size increases so does the standard deviation of the difference in hit positions. The MCPs will have a detection resolution of ≈ 1 mm, which will have some broadening effect compared to the simulations, which assume perfect detection resolution.

From both Figure 4.8(a) and Figure 4.8(b) the $\beta\alpha$ channel sits above the βp channel. The $\beta\alpha$ decay channel is imparted significantly more kinetic energy as the Q-value is much greater, meaning the emitter has a greater relative velocity. The reference frame of the

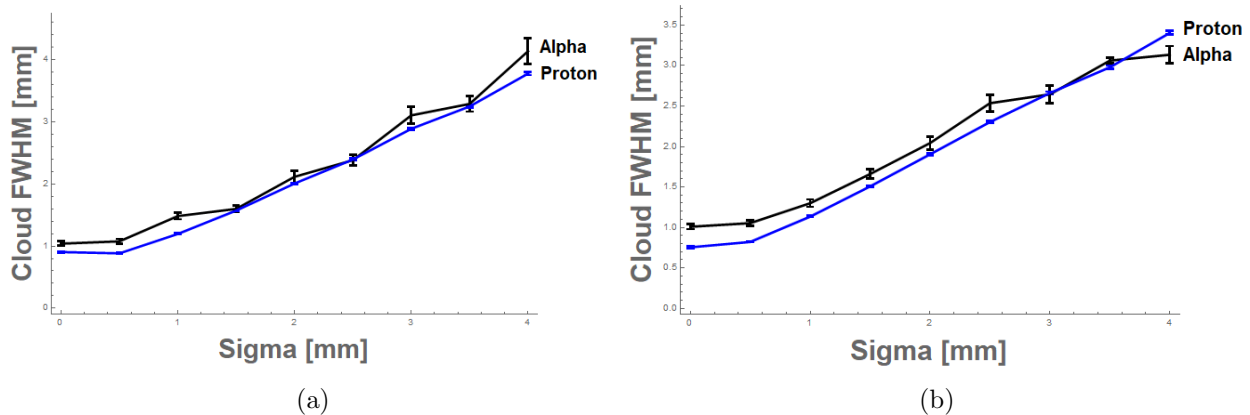


Figure 4.8: Simulated Comparison of the standard deviation of the detected difference in hit position with varying ion cloud size for the MCP detectors along the x-axis (a.) and y-axis (b.)

$\beta\alpha$ channel is therefore moving at a greater velocity, and the angle between the α particle and lithium atom will be greater than the angle between the proton and ^{10}Be for the βp channel from conservation of momentum. This relates to Figure 4.8 as with a greater angle between particles, the $\beta\alpha$ channel will naturally have a greater FWHM for the difference in hit positions compared to the βp channel. Furthermore, as the FWHM of the ion cloud increases, the difference between the $\beta\alpha$ and βp channel curves represented in Figure 4.8 diminishes. This results from a reduction in the recoil effect, or the effect of the velocity of the frame, the emitter, as the decays happen closer to the detector.

Figure 4.9 displays the change of the ToF differences for both the $\beta\alpha$ and βp channels as a function of the cloud size. The ToF differences depicted in Figure 4.9 for both channels create relatively straight lines, meaning if the cloud size increases such that it favors one side or another, the ToF difference remains nearly the same. Equation 4.1 depicts the ToF for the alpha decay with a small change in the location of the decay, ϵ .

$$\Delta T_{oF} = \left(\frac{1 \pm \epsilon}{v_{Li}} - \frac{1 \mp \epsilon}{v_{\alpha}} \right) d \quad (4.1)$$

In 4.1 the ϵ represents a small change, which favors one side or the other. The maximum size of the ion cloud in the simulation was 4.0 mm. The distance, d , of the center of the

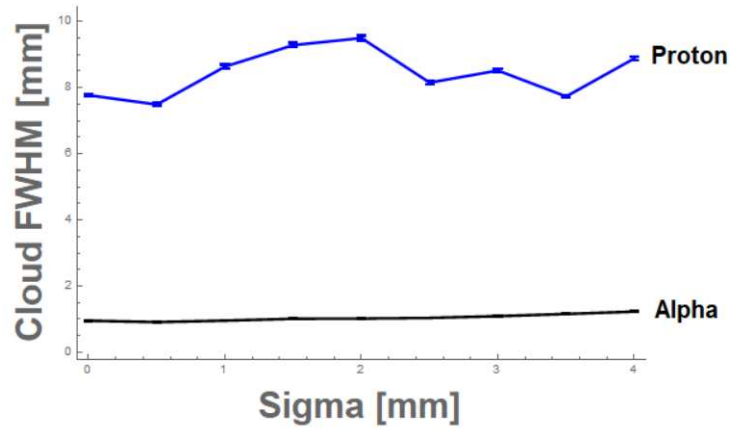


Figure 4.9: Simulated Comparison of the average ToF with varying ion cloud size

ion trap to an MCP is 70 mm. Therefore, in looking at the maximum change in the ToF average, ϵ should be $4.0 \text{ mm} / 70 \text{ mm} \approx 0.057$. Solving the equation for both cases, when favoring the α particle and when favoring the lithium atom, the difference is 1.725×10^{-8} . As the difference between the maximas is insignificant, so should any changes to the cloud size on the ToF differences.

CHAPTER 5

CONCLUSION

Nuclear halos provide a gateway into better understanding β -delayed particle emission and β decay in general. One very unique case of β -delayed particle emission is ^{11}Be as the branching ratios to the exotic states are greater than expected as a result of a nonspherical deformation in its core, ^{10}Be . The deformation is a product of competition between nucleon orbits which results in the ground state of ^{11}Be being an even parity, defying the expectations of the nuclear shell model. The first four states of ^{11}B , including the ground state, are odd parity or forbidden, making the branching ratios of the exotic states greater as a byproduct. Simulations were performed of the β -delayed decay of ^{11}Be in a linear Paul trap in order to verify the ToF difference profiles for each decay channel, the parameters of a kinematic cut to suppress the background coincidences and determine the influence of the cloud size on the detected difference in hit positions.

The decay was simulated following the decay rate equation given in ref [1], accounting for all of the angular correlations between the emitted particles. This included the determination and verification of the energy distributions of each of the emitted particles using the toolkit ROOT. The linear Paul trap was constructed in the simulation toolkit GEANT4. The ToF difference profiles were determined by taking the difference in the ToFs of the daughter atoms and the emitted particles. The parameters of the kinematic cut were determined by ensuring back-to-back hit positions in order to preferentially select the β -delayed channels. Lastly, the influence of the cloud size was determined by incrementally increasing the cloud size and studying its impact on the detected difference in hit positions.

The ToF difference peaks matched expectations, verified by calculation using the average energies of the emitted particles and the geometry of the BeTrap. The simulations demonstrate clear differentiation of the ToF difference profiles and evidence an ability to discern

which decay channel is being observed. The kinematic cut parameters were determined and functioned to reduce the rate of random coincidences. This reduction allows for better identification of the β -delayed channels. The detected difference in hit positions was determined as a function of the ion cloud size. During experimentation, the simulation could provide the expected cloud size given a detected spatial distribution. This will help in the diagnosis of how well the ion cloud is trapped. The next step is carrying out experimentation and comparing the results to the simulation. In the case of the kinematic cut and cloud size analysis, both can be used to aid experimentation by giving the parameters for reducing the random coincidences and expressing how well the BeTrap is trapping the ion cloud.

REFERENCES CITED

- [1] Barry R. Holstein. Recoil effects in allowed beta decay: The elementary particle approach. *Rev. Mod. Phys.*, **46**:789–814, Oct 1974. doi: 10.1103/RevModPhys.46.789. URL <https://link.aps.org/doi/10.1103/RevModPhys.46.789>.
- [2] T. Misu, W. Nazarewicz, and S. Åberg. Deformed nuclear halos. *Nuclear Physics A*, **614**(1):44 – 70, 1997. ISSN 0375-9474. doi: [https://doi.org/10.1016/S0375-9474\(96\)00458-7](https://doi.org/10.1016/S0375-9474(96)00458-7). URL <http://www.sciencedirect.com/science/article/pii/S0375947496004587>.
- [3] Aaron Gallant. Direct measurement of the beta-delayed proton branch in ^{11}Be using a new ion trap at TITAN for charged particle spectroscopy. *TRIUMF EEC New Research Proposal*, **2047**.
- [4] Kenneth S. Krane. *Introductory Nuclear Physics*. John Wiley and Sons, 3 edition, 1988. ISBN 047180553X.
- [5] Kyle G. Leach. *Neutron Transfer Reactions on ^{64}Zn as a Probe for Testing Shell-Model Isospin-Symmetry-Breaking Theory*. PhD thesis, The University of Guelph, Guelph and Ontario and Canada, 2012.
- [6] Conservation of Baryon Number. <http://hyperphysics.phy-astr.gsu.edu/hbase/Particles/parint.html>, .
- [7] Mark T. Lusk. Time-Dependent Perturbation Theory. *Colorado School of Mines*, 2019.
- [8] Wilson and Fred L. Fermi’s Theory of Beta Decay. *American Journal of Physics*, **36** (12):1150–1160, 1968.
- [9] Robley D. Evans. *The Atomic Nucleus*. McGraw-Hill, 1955. ISBN 0898744148.
- [10] H. Behrens and J. Janecke. Numerical Data and Functional Relationships in Science and Technology. *Landolt-Bornstien*, **4**, 1969.
- [11] M. Pfützner, M. Karny, L. V. Grigorenko, and K. Riisager. Radioactive decays at limits of nuclear stability. *Rev. Mod. Phys.*, **84**:567–619, Apr 2012. doi: 10.1103/RevModPhys.84.567. URL <https://link.aps.org/doi/10.1103/RevModPhys.84.567>.

- [12] M J G Borge. Beta-delayed particle emission. *Physica Scripta*, **T152**:014013, jan 2013. doi: 10.1088/0031-8949/2013/t152/014013. URL <https://doi.org/10.1088/2F0031-8949%2F2013%2Ft152%2F014013>.
- [13] K. Riisager, O. Forstner, M.J.G. Borge, J.A. Briz, M. Carmona-Gallardo, L.M. Fraile, H.O.U. Fynbo, T. Giles, A. Gottberg, A. Heinz, J.G. Johansen, B. Jonson, J. Kurcewicz, M.V. Lund, T. Nilsson, G. Nyman, E. Rapisarda, P. Steier, O. Tengblad, R. Thies, and S.R. Winkler. Be11(p), a quasi-free neutron decay? *Physics Letters B*, **732**:305 – 308, 2014. ISSN 0370-2693. doi: <https://doi.org/10.1016/j.physletb.2014.03.062>. URL <http://www.sciencedirect.com/science/article/pii/S0370269314002299>.
- [14] Isao Tanihata. Neutron halo nuclei. *J. Phys. G*, **22**:157–198, 1996. doi: 10.1088/0954-3899/22/2/004.
- [15] M. Fukuda, T. Ichihara, N. Inabe, T. Kubo, H. Kumagai, T. Nakagawa, Y. Yano, I. Tanihata, M. Adachi, K. Asahi, M. Kouguchi, M. Ishihara, H. Sagawa, and S. Shimoura. Neutron halo in ^{11}Be studied via reaction cross sections. *Physics Letters B*, **268**:339–344, 1991. doi: 10.1016/0370-2693(91)91587-L.
- [16] D.E. Alburger and D.H. Wilkinson. Decay of ^{11}Be . *Physical Review C*, **3**, 1492, 1971.
- [17] I Talmi and I Unna. Order of levels in the shell model and spin of ^{11}be . *Phys. Rev. Letters*. doi: 10.1103/PhysRevLett.4.469.
- [18] D. E. Alburger, D. J. Millener, and D. H. Wilkinson. Delayed particles from the beta decay of ^{11}Be . *Phys. Rev. C*, **23**:473–479, Jan 1981. doi: 10.1103/PhysRevC.23.473. URL <https://link.aps.org/doi/10.1103/PhysRevC.23.473>.
- [19] M. Bouten, E. Flerackers, and M.C. Bouten. Positive-parity states in odd p-shell nuclei. *Nuclear Physics A*, **307**(3):413 – 420, 1978. ISSN 0375-9474. doi: [https://doi.org/10.1016/0375-9474\(78\)90456-6](https://doi.org/10.1016/0375-9474(78)90456-6). URL <http://www.sciencedirect.com/science/article/pii/0375947478904566>.
- [20] C. David Sherrill. An introduction to Hartree-Fock Molecular Orbital Theory. *Georgia Institute of Technology*, 2000.
- [21] J. Refsgaard, J. Büscher, A. Arokiaraj, H. O. U. Fynbo, R. Raabe, and K. Riisager. Clarification of large-strength transitions in the β decay of ^{11}Be . *Phys. Rev. C*, **99**: 044316, Apr 2019. doi: 10.1103/PhysRevC.99.044316. URL <https://link.aps.org/doi/10.1103/PhysRevC.99.044316>.

- [22] S.M.Lukyanov, A.S. Denikin, E.I. Voskoboynik, S.V. Khlebnikov, M.N. Harakeh, Yu E. Penionzhkevich, Yu G. Sobolev, W.H. Trzaska, G.P. Tyurin, and K.A. Kuterbekov. Study of internal structures of $^9,^{10}\text{Be}$ and ^{10}B in scattering of ^4He from ^9Be . *Journal of Physics G: Nuclear and Particle Physics*, **41**(3):035102, 2014.
- [23] A.H. Wapstra, G. Audi, and C. Thibault. The AME2003 atomic mass evaluation. *Nuclear Physics A*, **729**:129–336, 2003.
- [24] Y. Ayyad, B. Olaizola, W. Mittig, G. Potel, V. Zelevinsky, M. Horoi, S. Beceiro-Novo, M. Alcorta, C. Andreouiu, T. Ahn, M. Anholm, , L. Atar, A. Babu, D. Bazin, N. Bernier, S. S. Bhattacharjee, M. Bowry, R. Caballero-Folch, M. Cortesi, C. Dalitz, E. Dunling, A. B. Garnsworthy, M. Holl, B. Kootte, K. G. Leach, J. S. Randhawa, Y. Saito, C. Santamaria, P. Siuryte, C. E. Svensson, R. Umashankar, N. Watwood, and D. Yates. Direct observation of proton emission in ^{11}Be . *Physical Review Letter*, **123**, 082501, 2019.
- [25] K. Riisager, M.J.G. Borge, J.A. Briz, M. Carmona-Gallardo, O. Forstner, L.M. Fraile, H.O.U. Fynbo, A. Garzon Camacho, J.G. Johansen, B. Jonson, M.V. Lund, J. Lachner, M. Madurga, S. Merchel, E. Nacher, T. Nilsson, P. Steier, O. Tengblad, and V. Vedia. Search for beta-delayed proton emission from ^{11}Be . *The European Physical Journal A*, **56**(3):100, 2020.
- [26] K. Siegl, N. D. Scielzo, A. Czeszumaska, J. A. Clark, G. Savard, A. Aprahamian, S. A. Caldwell, B. S. Alan, M. T. Burkey, C. J. Chiara, J. P. Greene, J. Harker, S. T. Marley, G. E. Morgan, J. M. Munson, E. B. Norman, R. Orford, S. Padgett, A. Perez Galván, K. S. Sharma, and S. Y. Strauss. Recoil ions from the β decay of ^{134}Sb confined in a paul trap. *Phys. Rev. C*, **97**:035504, Mar 2018. doi: 10.1103/PhysRevC.97.035504. URL <https://link.aps.org/doi/10.1103/PhysRevC.97.035504>.
- [27] R.M. Yee, N.D. Scielzo, P.F. Bertone, F. Buchinger, S. Caldwell, J.A. Clark, C.M. Deibel, J. Fallis, J.P. Greene, S. Gulick, D. Lascar, A.F. Levand, G. Li, E.B. Norman, M. Pedretti, G. Savard, R.E. Segel, K.S. Sjar anda, M.G. Stermberg, J. Van Schelt, and B.J. Zabransky. β -Delayed Neutron Spectroscopy Using Trapped Radioactive Ions. *Physical Review Letters*, **110**, 9:092501, 2013.
- [28] Tommi Eronen, Anu Kankainen, and Juha Äystö. Ion traps in nuclear physics—recent results and achievements. *Progress in Particle and Nuclear Physics*, **91**:259 – 293, 2016. ISSN 0146-6410. doi: <https://doi.org/10.1016/j.pnnp.2016.08.001>. URL <http://www.sciencedirect.com/science/article/pii/S0146641016300436>.

- [29] N. Scielzo, Gang Li, Matthew Sternberg, G. Savard, P.F. Bertone, Fritz Buchinger, Salen Caldwell, J. Clark, John Crawford, Catherine Deibel, Jennifer Fallis, John Greene, S. Gulick, A. Hecht, D. Lascar, J.K.P. Lee, A.F. Levand, M. Pedretti, R.E. Segel, and B. Zabransky. The β -decay-decay paul trap: A radiofrequency-quadrupole ion trap for precision β -decay-decay studies. *Nuclear Instruments and Methods in Physics Research Section A: Accelerators, Spectrometers, Detectors and Associated Equipment*, **681**:94–100, 07 2012. doi: 10.1016/j.nima.2012.04.035.
- [30] Richard C. Thompson, Niels Madsen, and Martina Knoop. *Trapped Charged Particles*. WSPC, 1 edition, 2016. ISBN 1786340127.
- [31] S. Schwarz. Simulations for ion traps buffer gas cooling. *Lecture Notes in Physics*, **749**: 1–21, 11 2008. doi: 10.1007/978-3-540-77817-2_4.
- [32] A. Nieminen, P. Campbell, J. Billowes, D. H. Forest, J. A. R. Griffith, J. Huikari, A. Jokinen, I. D. Moore, R. Moore, G. Tungate, and J. Äystö. On-line ion cooling and bunching for collinear laser spectroscopy. *Phys. Rev. Lett.*, **88**:094801, Feb 2002. doi: 10.1103/PhysRevLett.88.094801. URL <https://link.aps.org/doi/10.1103/PhysRevLett.88.094801>.
- [33] F.G. Major and H.G. Dehmelt. Exchange-Collision Technique for the rf Spectroscopy of Stored Ions. *Physical Review*, **170**(1):91–107, 1968.
- [34] F.G. Major, V.N. Gheorghe, and G. Werth. *Charged Particle Traps*. 37. Springer-Verlag Berlin Heidelberg, 2005. ISBN 3540220437.
- [35] L.S. Cutler, R.P. Giffard, and M.D. McGuire. Thermalization of ^{199}Hg Ion Macromotion by a Light Background Gas in an RF Quadrupole Trap. *Applied Physics B*, **36**:137–142, 1985.
- [36] Wolfgang Paul. Electromagnetic traps for charged and neutral particles. *Rev. Mod. Phys.*, **62**:531–540, Jul 1990. doi: 10.1103/RevModPhys.62.531. URL <https://link.aps.org/doi/10.1103/RevModPhys.62.531>.
- [37] Phillip Wieburg. A Linear Paul Trap for Ytterbium Ions. Master’s thesis, Universität Hamburg, 2014.
- [38] Stephan Timo Gulde. *Experimental Realization of Quantum Gates and the Deutsch-Jozsa Algorithm with Trapped $^{40}\text{Ca}^+$ Ions*. PhD thesis, 2003.
- [39] Microchannel plate (MCP) detectors. https://www.atom.uni-frankfurt.de/research/10_COLTRIMS/20_MCP-detectors/, .
- [40] Microchannel Plates. https://www.rp-photonics.com/microchannel_plates.html, .

- [41] Ryan C. Blase, Roland R. Benke, Chathan M. Cooke, and Keith S. Pickens. Microchannel Plate Detector Detection Efficiency to Monoenergetic Electrons Between 0.4 and 2.6 MeV. *IEEE Transactions on Nuclear Science*, **62**(6):3339–3345, 2015.
- [42] J Oberheide, P Wilhelms, and M Zimmer. New results on the absolute ion detection efficiencies of a microchannel plate. *Measurement Science and Technology*, **8**(4):351–354, apr 1997. doi: 10.1088/0957-0233/8/4/001. URL <https://doi.org/10.1088/0957-0233/8/4/001>.
- [43] Ryan C. Blase, Roland R. Benke, Gregory P. Miller, Keith S. Pickens, and J. Hunter Waite. Microchannel plate detector detection efficiency to monoenergetic electrons between 3 and 28 keV. *Review of Scientific Instruments*, **88**(5):053302, 2017. doi: 10.1063/1.4983338. URL <https://doi.org/10.1063/1.4983338>.
- [44] S. Carboni, S. Barlini, L. Bardelli, N. Le Neindre, M. Bini, B. Borderie, R. Bougault, G. Casini, P. Edelbruck, A. Olmi, G. Pasquali, G. Poggi, M.F. Rivet, A.A. Stefanini, G. Baiocco, R. Berjillos, E. Bonnet, M. Bruno, A. Chbihi, I. Crucecu, M. Degerlier, J.A. Due as, E. Galichet, F. Gramegna, A. Kordyasz, T. Kozik, V.L. Kravchuk, O. Lopez, T. Marchi, I. Martel, L. Morelli, M. Parlog, H. Petrascu, E. Rosato, V. Sere-dov, E. Vient, M. Vigilante, R. Alba, D. Santonocito, and C. Maiolino. Particle identification using the $\delta e - e$ technique and pulse shape discrimination with the silicon detectors of the FAZIA project. *Nuclear Instruments and Methods in Physics Research A*, **664**:251–263, 2012.
- [45] About Geant4. https://geant4.web.cern.ch/support/getting_started/about_geant4, .
- [46] Anna Zaborowska. Geant4 Full and Fast Simulation Framework. https://indico.cern.ch/event/438866/contributions/1085071/attachments/1257812/1857574/Zaborowska_FCCGeantSim.pdf, 2016.
- [47] ROOT. <https://root.cern.ch>, .
- [48] Cubic Spline. <https://mathworld.wolfram.com/CubicSpline.html>, .
- [49] P Descouvemont and D Baye. The R-matrix theory. *Reports on Progress in Physics*, **73**(3):036301, feb 2010. doi: 10.1088/0034-4885/73/3/036301. URL <https://doi.org/10.1088/0034-4885/73/3/036301>.
- [50] Alexander Volya. Assessment of the beta-delayed proton decay rate of ^{11}Be . 2 2020.

- [51] S. Kox, A. Gamp, C. Perrin, J. Arvieux, R. Bertholet, J. F. Bruandet, M. Buenerd, R. Cherkaoui, A. J. Cole, Y. El-Masri, N. Longequeue, J. Menet, F. Merchex, and J. B. Viano. Trends of total reaction cross sections for heavy ion collisions in the intermediate energy range. *Physical Review C*, **35**, 5:1678–91, 1987.
- [52] S. RAMAN, C.W. NESTOR, and P. TIKKANEN. Transition probability from the ground to the first-excited $2+$ state of even-even nuclides. *Atomic Data and Nuclear Data Tables*, **78**(1):1 – 128, 2001. ISSN 0092-640X. doi: <https://doi.org/10.1006/adnd.2001.0858>. URL <http://www.sciencedirect.com/science/article/pii/S0092640X01908587>.
- [53] Electric Quadrupole Moments of Nuclei. <http://hyperphysics.phy-astr.gsu.edu/hbase/Nuclear/elequad.html>, .
- [54] J. D. Prestage, G. J. Dick, and L. Maleki. New ion trap for frequency standard applications. *Journal of Applied Physics*, **66**(3):1013–1017, 1989. doi: 10.1063/1.343486. URL <https://doi.org/10.1063/1.343486>.

APPENDIX A

DERIVATION OF THE ENERGY OF THE NEUTRINO AND β -DELAYED PARTICLE

A.1 Derivation of the neutrino energy

First begin with the conservation of 4-momentum where $P = \{E, \vec{p}\}$.

$$P_{parent} = P_{recoil} + P_{\beta} + P_{\nu} \quad (\text{A.1})$$

$$P_{Be} = P_B + P_{\beta} + P_{\nu} \quad (\text{A.2})$$

Solve for the recoil, ^{11}B and square both sides.

$$P_B = P_{Be} - P_{\beta} - P_{\nu} \quad (\text{A.3})$$

$$P_B^2 = (P_{Be} - P_{\beta} - P_{\nu})^2 \quad (\text{A.4})$$

The square of the 4-momentum of any particle is just the rest mass.

$$m_B^2 = m_{Be}^2 + m_{\beta}^2 + m_{\nu}^2 - 2(P_{Be} \cdot P_{\beta}) - 2(P_{Be} \cdot P_{\nu}) + 2(P_{\beta} \cdot P_{\nu}) \quad (\text{A.5})$$

Assume the system is in the rest frame of the parent, ^{11}Be .

$$m_B^2 - m_{Be}^2 - m_{\beta}^2 = -2(m_{Be}E_{\beta}) - 2(m_{Be}E_{\nu}) + 2(E_{\beta}E_{\nu} - \vec{p}_{\beta} \cdot \vec{p}_{\nu}) \quad (\text{A.6})$$

The absolute value of the momentum of the neutrino is its energy.

$$m_B^2 - m_{Be}^2 - m_{\beta}^2 = -2(m_{Be}E_{\beta}) - 2(m_{Be}E_{\nu}) + 2(E_{\beta}E_{\nu} - \vec{p}_{\beta} \cdot E_{\nu}\hat{p}_{\nu}) \quad (\text{A.7})$$

Therefore we can conclude the energy of the neutrino to be the following,

$$E_{\nu} = \frac{m_B^2 - m_{Be}^2 - m_{\beta}^2 + 2(m_{Be}E_{\beta})}{2(E_{\beta} - m_{Be} - \vec{p}_{\beta} \cdot \hat{p}_{\nu})} \quad (\text{A.8})$$

A.2 Derivation of the energy of the β -delayed particle

First, begin with the conservation of 4-momentum, where $P = \{E, \vec{p}\}$.

$$P_{parent} = P_{recoil} + P_{emitted} \quad (\text{A.9})$$

Solve for the recoil 4-momentum and square both sides.

$$P_{recoil} = P_{emitted} - P_{parent} \quad (\text{A.10})$$

$$P_{recoil}^2 = (P_{emitted} - P_{parent})^2 \quad (\text{A.11})$$

This allows for a simplification using the identity $E^2 = \vec{p}^2 + m^2$ (assuming natural units).

$$m_{recoil}^2 = m_{parent}^2 + m_{emitted}^2 - 2(P_{recoil} \cdot P_{emitted}) \quad (\text{A.12})$$

Assuming the system takes place in the rest frame of the parent.

$$m_{recoil}^2 = m_{parent}^2 + m_{emitted}^2 - 2(m_{recoil}E_{emitted}) \quad (\text{A.13})$$

Therefore the energy of the emitted particle is the following,

$$E_{emitted} = \frac{m_{parent}^2 + m_{emitted}^2 - m_{recoil}^2}{2m_{parent}} \quad (\text{A.14})$$

APPENDIX B

DETAILS ON THE CONFIRMATION OF THE HALO STRUCTURE OF ^{11}Be

The structure of ^{11}Be was confirmed by studying the reaction cross sections [15]. Comparing the experimental data gathered at 33.0 A MeV to the model developed in ref [51], the reaction cross section was found to be larger by 20%-30% [15, 51]. Figure B.1 depicts the experimental data of the cross section of ^{11}Be and various fits [15].

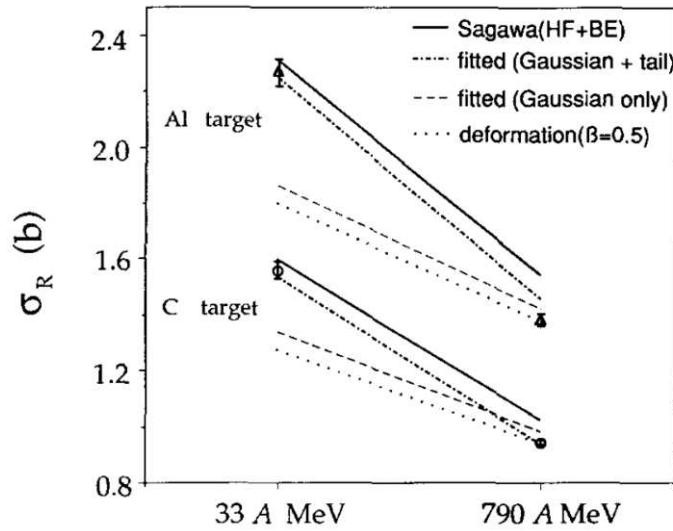


Figure B.1: Comparison of cross sections: Dash-dotted line: the best fitted gaussian plus Yukawa-square tail density distribution. Solid line: Hartree-Fock density with a binding-energy condition for ^{11}Be . Dashed line: deformed ^{11}B density ($\beta = 0.5$). Long dashed line: best fitted by a gaussian density distribution. Adopted from ref [15]

Figure B.1 shows the necessity in including a long tail in the nucleon distribution to explain the cross sections [15]. However, the halo structure doesn't fully encapsulate the cross section of ^{11}Be , as its core, ^{10}Be also has a nonspherical shape or a shape deformation [2]. The importance of the deformation can be depicted by the large quadrupole moment of its core ^{10}Be , $|Q| = 0.230 \text{ mb}$, which indicates a non-spherically symmetric charge distribution [52, 53].

APPENDIX C

DETAILED ANALYSIS OF A SPECTRAL FUNCTION

Equation C.1 is an example of a spectral function found within Equation 1.13.

$$\begin{aligned}
g_{12}(E, u, v, s) &= -\theta_{u,v} \text{Rec}_1^* [c_1 + 2c_2(1/M^2)(m_e^2 + 2EE_0 - 2E^2) \\
&\quad - (E_0/2M)(c_1 + d \pm b) + (E/M)(3c_1 \pm b) \\
&\quad - (m_e^2/2M^2)(1 + \Delta/2M)h] \\
&\quad - \delta_{u,v} \left(\frac{u(u+1)}{(2u-1)(2u+3)} \right)^{1/2} \text{Rea}_1^* \left[\left(\frac{3}{2} \right)^{1/2} f(E_0/M) \right. \\
&\quad \left. + 3g \frac{EE_0 - E^2}{2M^2} \pm \left(\frac{3}{2} \right)^{1/2} j_2 \frac{E_0^2 - 2EE_0 + m_e^2}{2M^2} \right] \\
&\quad + \kappa_{u,v}(-)^s \text{Rec}_1^* \left[\pm 3f \frac{E_0 - 2E}{2M} \right. \\
&\quad \left. \pm \left(\frac{3}{2} \right)^{1/2} g \frac{E_0^2 - 2EE_0 + m_e^2}{2M^2} \right. \\
&\quad \left. - j_2 \frac{-E_0^2 + 8EE_0 - 8E^2 + m_e^2}{4M^2} \right] \\
&\quad + \epsilon_{u,v} \text{Rec}_1^* j_3 \frac{E_0^2 + 9EE_0 - m_e^2 - 9E^2}{4M^2}
\end{aligned} \tag{C.1}$$

where,

$$\theta_{u,v} = \begin{cases} -(u+1)/(2u-1) & u = v + 1 \\ 1 & u = v \\ -u/(2u+3) & u = v - 1 \end{cases} \tag{C.2}$$

From Equation C.1, E is the energy of the electron, u is the spin of the precursor, v is the spin of the emitter and s is the spin of the daughter [1]. In order to have a better physical understanding, it is valuable to describe some of the physical interaction variables: a is the Fermi transition, b is weak magnetism, c is Gamow-Teller, d is the induced tensor, e is the induced scalar, etc. However, for each of the previous terms listed all but one is eliminated. For every term from Equation C.1, each incorporates one or more of the factors presented

in Table C.1 with the exception of the first line.

Factor	Value
E^2/M^2	9.49×10^{-9}
$E_0 E/M^2$	2.70×10^{-8}
m_e^2/M^2	2.48×10^{-9}
E_0/M	2.77×10^{-4}
E/M	9.74×10^{-5}

Table C.1: Factors incorporated in the majority of terms in Equation C.1

The maximum factor from Table C.1 is 9.74×10^{-5} . In the first term of the first line in Equation C.1, $-\theta_{u,v} Rec_1^* c_1 = -1$. The ratio of the largest possible factor present in every other term to the first term of Equation C.1 is 2.77×10^{-4} . For the purposes of this thesis these terms can be safely ignored.

APPENDIX D

DISCUSSION OF THE LINEAR PAUL TRAP'S EFFECT ON THE SECOND-ORDER DOPPLER SHIFT EFFECTS

In high accuracy measurements, the largest source of frequency offset results from the motion of the atoms caused by the trapping fields via the second-order Doppler effect [54]. This places a limitation on the number of ions that can be accurately measured in an ion trap. However, as mentioned previously, one of the big advantages of using a linear Paul trap is the reduction of the second-order Doppler shift [54]. Equation D.1 depicts the second-order Doppler shift where N is the total ion number and L is the trap length [54].

$$\left(\frac{\Delta f}{f}\right)_{lin} = -\left(\frac{q^2}{8\pi\epsilon_0 mc^2}\right)\frac{N}{L} \quad (\text{D.1})$$

What is important to note for Equation D.1 is the expression has no dependence on trap parameters except the linear ion density N/L [54]. Assuming the driving frequency is properly scaled, the linear trap holds 15 to 20 times more ions than a spherical trap with negligible increase to the second-order increase to the second-order Doppler shift [54].

APPENDIX E

βp DELAYED DECAY CHANNEL HISTOGRAMS

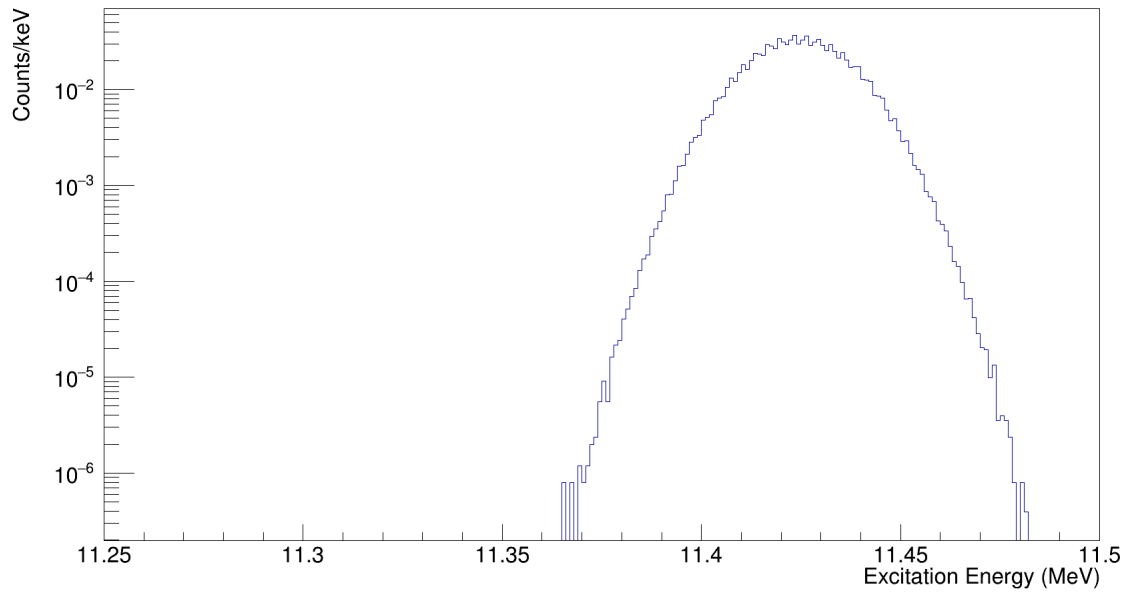


Figure E.1: Simulated distribution of excitation energy for the βp decay channel

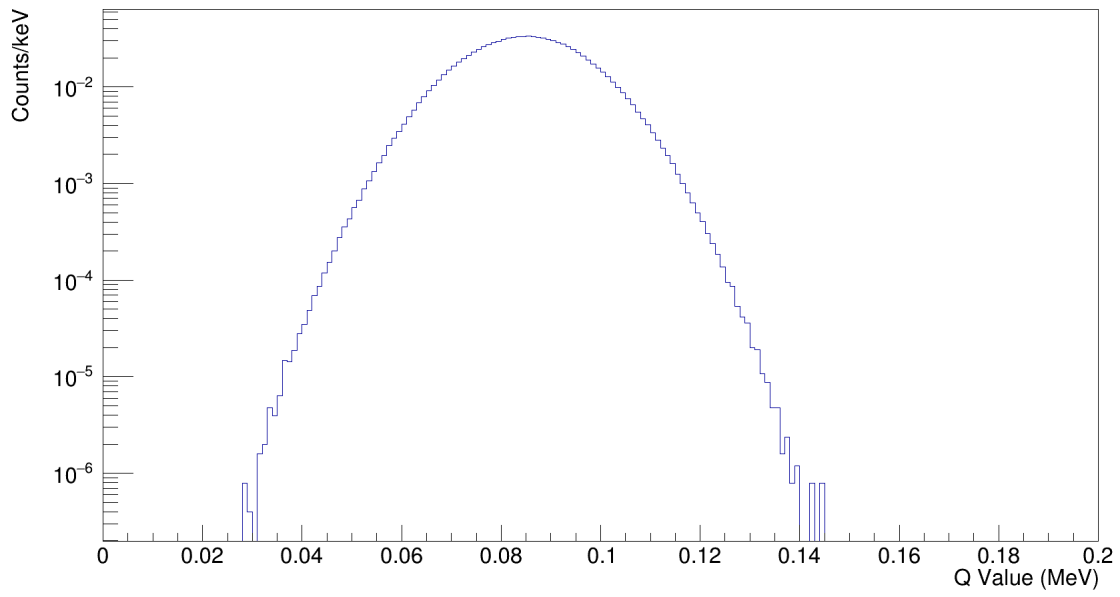


Figure E.2: Simulated distribution of Q-value for the βp decay channel

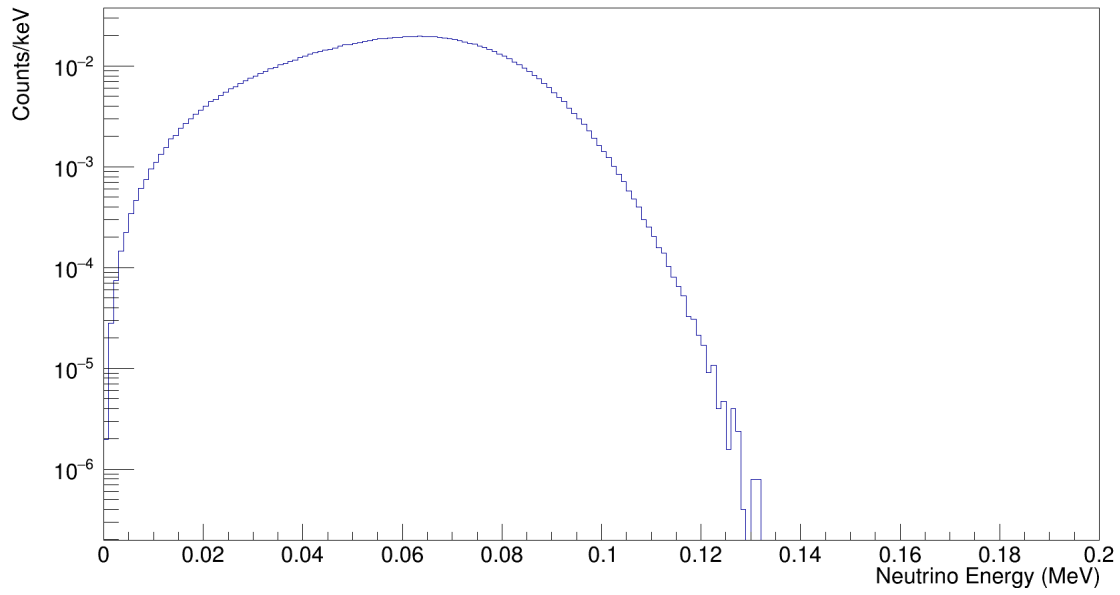


Figure E.3: Simulated distribution of neutrino energy for the βp decay channel

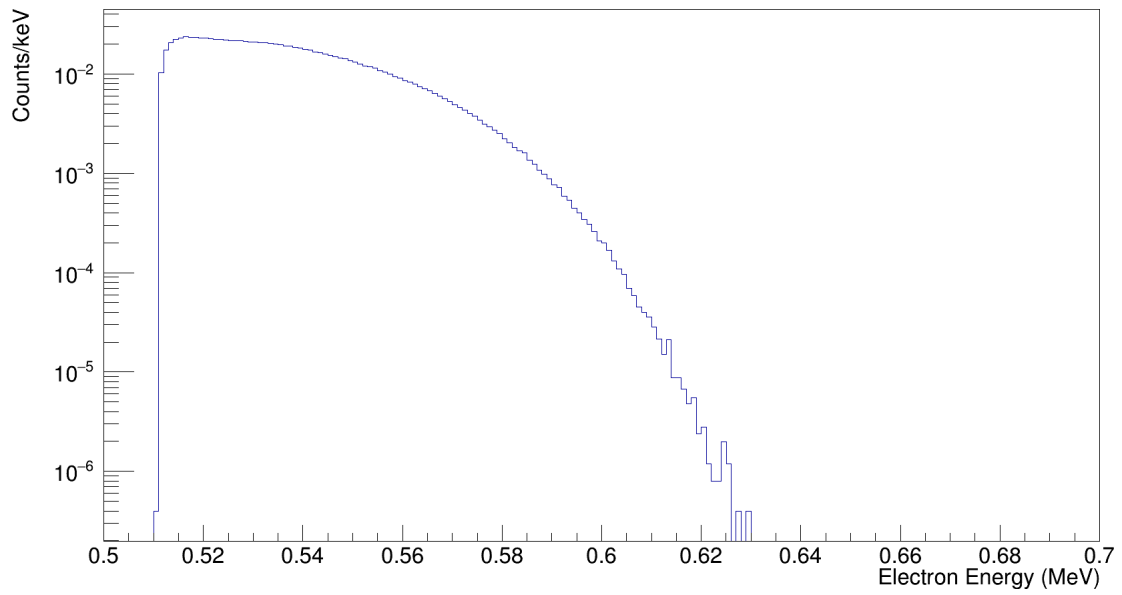


Figure E.4: Simulated distribution of electron energy for the βp decay channel

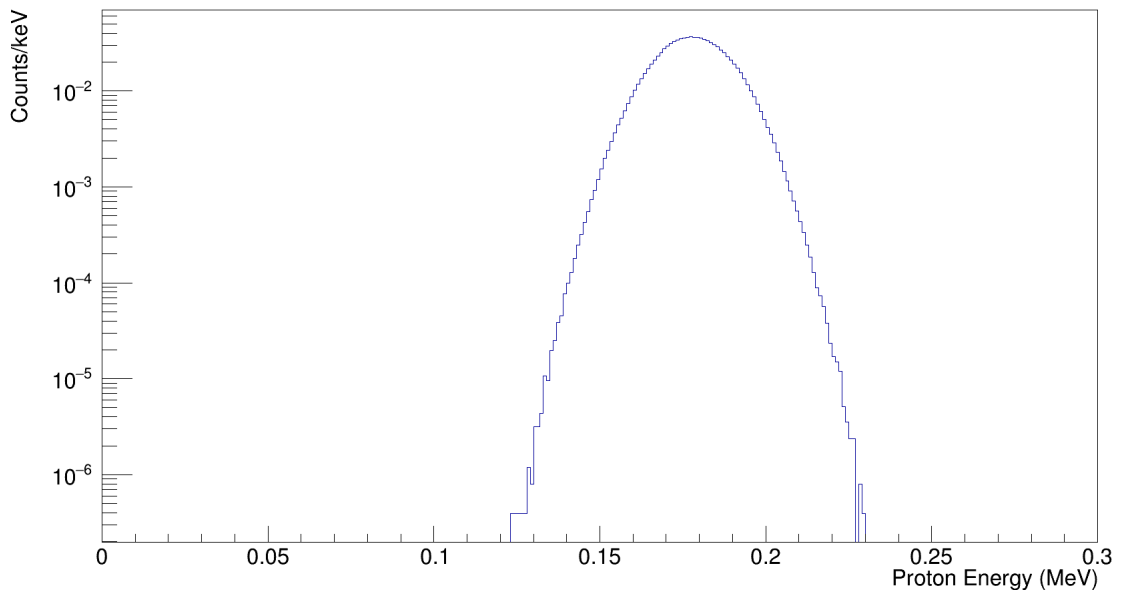


Figure E.5: Simulated distribution of proton energy for the βp decay channel

APPENDIX F
DISCUSSION OF $\beta\alpha$ TOF DIFFERENCE PROFILE

Figure F.1 depicts the difference in the simulated distribution in ToF difference profiles for the $\beta\alpha$ channel for the ground and excited state of the daughter atom, ${}^7\text{Li}$.

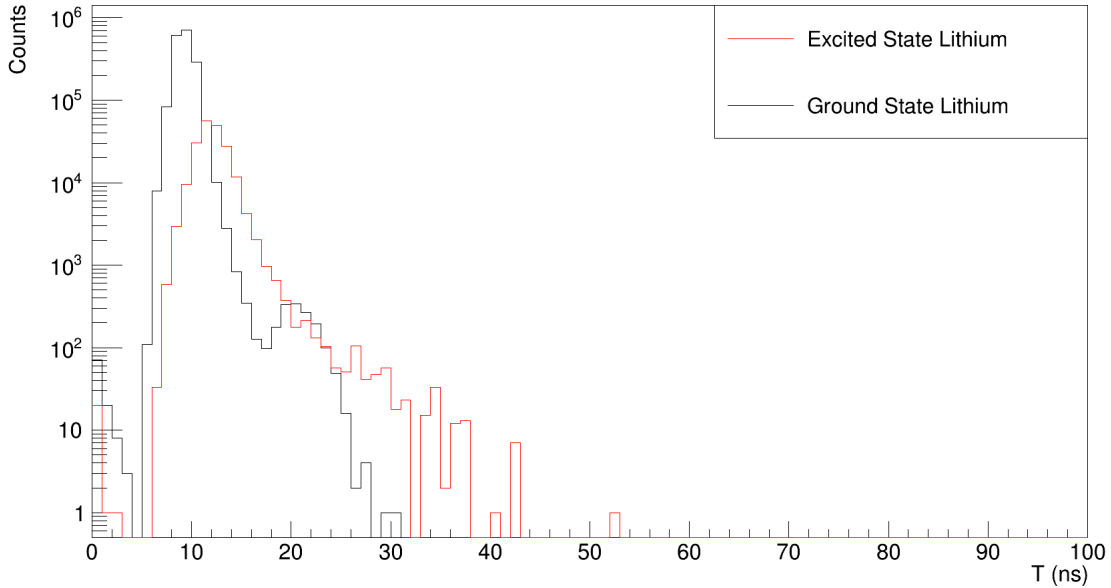


Figure F.1: Simulated distribution of ToF difference profile for the $\beta\alpha$ channel

One assumption may be there should exist two peaks in the profile depicted in Figure 4.1; however, because the average ToF differences between the ground and excited states of lithium are close, there is just broadening. The difference between the profiles in Figure F.1 stems from the excitation energy of the daughter atom, ${}^7\text{Li}$, resulting in an average ToF difference of 9.32 ns and 12.18 ns for the ground and excited states, respectively. The emitter can only α decay to an energetically possible state of the daughter and for an α decay to the excited state of the daughter, the excitation energy of the emitter must exceed 9.142 MeV. Near this threshold the Q-value for the α decay is relatively small, meaning the energy imparted to the decay particles is relatively small as well. This can affect the ToF

difference of the $\beta\alpha$ channel drastically. Take for example an emitter excitation energy of 9.15 MeV. The resulting Q-value of the α decay is 7.68 keV which produces a ToF difference between the α particle and lithium atom of approximately 108.4 ns. The counts heavily exceeding the average ToF difference for the $\beta\alpha$ channel result from an excitation energy of the emitter near the threshold.

From Figure F.1, another peak exists, centered at 21 ns. This results from electron-daughter atom coincidences from the $\beta\alpha$ channel. As mentioned in chapter 4, the average ToF for an electron is approximately 0.12 ns, while the average ToF for the ${}^7\text{Li}$ is 21 ns. The average difference between the ToFs for an electron and ${}^7\text{Li}$ atom is therefore roughly 21 ns.